Final Report
August 2018

Determining the Effects of Cross-Anisotropy on Pavement Response and Performance

SOLARIS Consortium, Tier 1 University Transportation Center
Center for Advanced Transportation Education and Research
Department of Civil and Environmental Engineering
University of Nevada, Reno
Reno, NV 89557

Rafiqul Tarefder, Ph.D., P.E.
Mesbah Ahmed, Ph.D.
Department of Civil Engineering
University of New Mexico; Albuquerque, NM 87131

***DISCLAIMER*:**

The contents of this report reflect the views of the authors, who are responsible for the facts and accuracy of the information presented herein. This document is disseminated under the sponsorship of the U.S. Department of Transportation's University Transportation Centers Program, in the interest of information exchange. The U.S. Government assumes no liability for the contents or use thereof.

SUMMARY PAGE

<table>
<tr><td colspan="2">1. Report No.</td><td colspan="2">2. Recipient’s Catalog No.</td></tr>
<tr><td colspan="2">3. Title and Subtitle
Determining the Effects of Cross-Anisotropy on Pavement Response and Performance</td><td colspan="2">4. Report Date
December 31, 2017</td></tr>
<tr><td colspan="2">5. Author(s):
Rafiqul A. Tarefder and Mesbah U. Ahmed</td><td colspan="2">6. Performing Organization Report No.</td></tr>
<tr><td colspan="2" rowspan="2">7. Performing Organization Name and Address
University of New Mexico
Department of Civil Engineering
MSC01 1070
1 University of New Mexico
Albuquerque, NM 87131</td><td colspan="2">8. Performing Organization Code</td></tr>
<tr><td colspan="2">9. Contract/Grant No.</td></tr>
<tr><td colspan="2" rowspan="2">10. Sponsoring Agency Name and Address
SOLARIS Institution, University Transportation Center</td><td colspan="2">11. Type of Report and Period Covered
Final Report</td></tr>
<tr><td colspan="2">12. Sponsoring Agency Code</td></tr>
<tr><td colspan="4">13. Supplementary Notes
The research project is funded by SOLARIS</td></tr>
<tr><td colspan="4">14. Abstract
This study is performed to investigate the effect of cross-anisotropy in Asphalt Concrete (AC) on pavement responses, i.e., stress-strain, and performance, i.e., damage due to fatigue and permanent deformation. To date, a full-scale Finite Element Model (FEM) of an instrumented pavement section is developed in ABAQUS 6-EF-2. Laboratory tests were conducted on AC cores and aggregates to inputs for material models: (a) cross-anisotropic and viscoelasticity for AC layer, and (b) nonlinear elasticity and stress-dependency for aggregate layers. The developed material models are integrated to ABAQUS via User Defined Material (UMAT) interface. The full-scale FEM is validated by comparing the simulated pavement responses with those measured by field instrumentation under a Falling Weight Deflectometer (FWD) test load. Later, a parametric study is performed by simulating the FEM at varying parameters such as degree of cross-anisotropy (n-value) in AC layer, pavement temperature, and so on. It is observed that the tensile strain at the bottom of AC layer and resulting fatigue damage increases whenever AC is cross-anisotropic. This effect is enhanced in presence of high pavement temperature, unbound layer cross-anisotropy, and nonlinearity. Vertical compressive strain as well as damage due to permanent deformation are also sensitive to AC cross-anisotropy and follows the similar type of trend. Effect of AC cross-anisotropy on these strains and damage are very high in unbound layers, specially, base and subbase. In addition, presence of high temperature and base layer cross-anisotropy. It is observed that variation in loading duration highly affects vertical strain and permanent deformation in pavement layers.</td></tr>
<tr><td colspan="2">15. Key Words
Asphalt Concrete, Cross-Anisotropy, FEM, Viscoelasticity, Stress-dependency, and Stress-strain</td><td colspan="2">16. Distribution Statement
No restrictions.</td></tr>
<tr><td>17. Security Classification of the Report
None</td><td>18. Security Classification of this page
None</td><td>19. Number of Pages
60</td><td>20. Price
N/A</td></tr>
</table>

TABLE OF CONTENTS

LIST OF TABLES

LIST OF FIGURES

INTRODUCTION

Compaction forces applied for compacting a pavement layer are equal in horizontal and vertical planes due to the lack of confinement in the horizontal plane. Materials' stiffness may vary along the vertical and horizontal directions due to this nature of compaction. An Asphalt Concrete (AC) layer can be be anisotropic since stiffness, i.e., defined by modulus of elasticity *E*-value throughout this report, is not same in three orthogonal directions. AC layer is assumed cross-anisotropic in this study, which is a special case of anisotropy where *E*-values along horizontal plane are the same, however, it differs in vertical direction (Lo and Lee 1990 and Tutumluer and Seyhan 1999). As shown in Figure 1, stiffness *E*-values (E_x and E_z) are same in horizontal plane, but not equal to the vertical *E*-value (E_y). In this study, the ratio of horizontal to vertical modulus of elasticity is defined as degree of cross-anisotropy (*n*-value), i.e., $n = E_x/E_y = E_h/E_v$, where, E_v and E_h are vertical and horizontal modulus respectively.

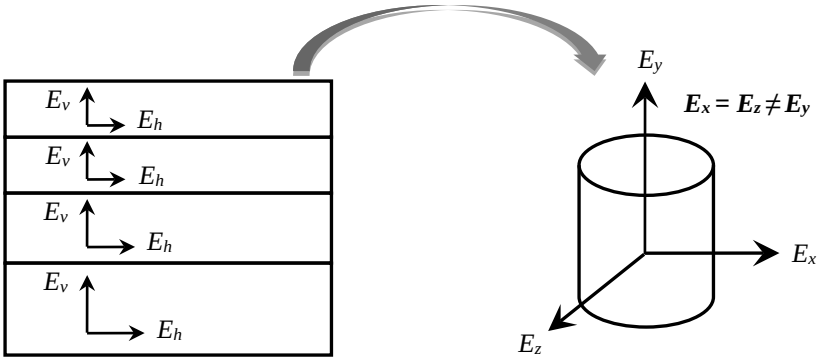

Figure 1: Cross-anisotropy in pavement materials

Till today, the conventional pavement ME design software assume AC as an isotropic material during stress-strain computation. An AC layer can be assumed as isotropic it exhibits identical stiffness along 3-orhtogonal directions. However, due to the nature of compaction in the field, AC layer is not isotropic, instead, it is cross-anisotropic (Masad et al. 2002 and Wang et al. 2005). Presence of cross-anisotropy in AC layer influences the pavement responses, i.e. stress-strain. Specifically, fatigue and rutting performances of AC pavements are related to stress-strain responses of pavements under load as imposed by traffic. There is a need for studying the effects of AC layer cross-anisotropy on pavement responses and predicted fatigue and rutting performances.

Most of the previous studies related to pavement responses and performances considered the cross-anisotropy of the unbound granular aggregate layer: base and subbase (Lo and Lee 1990, Tutumluer and Seyhan 1999, and Al-Qadi et al. 2010). Recently, few studies have reported the presence of cross-anisotropy in AC layer (Masad et al. 2002, Wang et al. 2005, Motola and Uzan 2007). A flexible pavement being a multilayered structure that comprises the stiffest material, i.e., Asphalt Concrete (AC), in top layer and gradually lesser stiff material, i.e., aggregates and soil, in bottom layers, the AC layer is directly under traffic loading and therefore is subjected to the highest amount of induced stress. Therefore, ignoring AC cross-anisotropy may cause significant error in predicting critical stress and strains, which are used to predict fatigue damage or permanent deformation of a pavement by pavement ME design. To date this study is

performed to understand the effect of AC cross-anisotropy on critical pavement responses and thereby, performances.

OBJECTIVES

Main goal of this study is to investigate the effect of cross-anisotropy on pavement responses, i.e., stress-strain, and thereby, performance, i.e., pavement damage, under repeated loading.

- Development of a full-scale Finite Element Model (FEM) of an instrumented pavement section to determine pavement responses, i.e., deflection, stress, and strain under dynamic load.
- Conduct laboratory tests to determine inputs for material models, i.e., viscoelasticity and stress-dependency for asphalt and aggregate layers respectively. In addition, integrate the material models into the full-scale FEM of pavement.
- Conduct field tests to measure in-situ stress-strain of instrumented pavement section and compare with those from the FEM simulation.
- Perform FEM simulations at varying degree of cross-anisotropy to investigate the effect of cross-anisotropy on pavement responses.
- Simulated strains at varying degree of cross-anisotropy will be incorporated to the mechanistic-empirical models to determine pavement performance, i.e., fatigue damage and permanent deformation.

TASK 1: DEVELOPMENT OF FINITE ELEMENT MODEL

Goal of this study is to investigate the effect of cross-anisotropy of flexible pavement layer materials on pavement responses, such as stress and strain. The Finite Element Analysis (FEA) is adopted to perform the mechanistic analysis to determine stress-strain. The basic equation of FEA is as follows:

$$\{F\} = [K]\{d\} \tag{1}$$

where $\{F\}$ = nodal force, $[K]$ = stiffness of an element, and $\{d\}$ = nodal displacement. Stiffness is defined by a force required to cause a unit deformation/displacement. For instance, a simple 1-D element with 2-nodes and 1-Degree of Freedom (DOF) has a 2 x 2 stiffness matrix (see Figure 2). Therefore, forces can be determined if the total displacements at the nodes are known and vice versa.

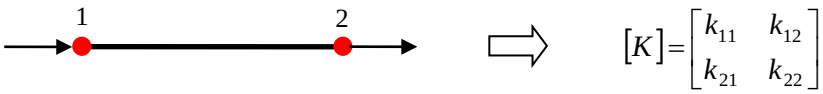

Figure 2: Basic stiffness matrix of a simple element

A typical FEA is not a simple element as shown in Figure 1. A domain or geometry of a specific FEA problem is divided or discretized into a number of elements with varying number of nodes and DOFs. Local stiffness matrices are developed for each the elements in a domain which are later assembled to generate a global stiffness matrix for the entire domain. Eqn. (1) is then used to solve the problem based on the global stiffness matrix.

A FEA is commonly implemented through a number of steps which are shown in Figure 3. Geometry needs to be developed based on available dimensions of an object/continuum which is to be modeled. Once the geometry is developed, mechanical properties of the continuum needs to be incorporated. For instance, modulus of elasticity (E) and Poisson's ratio (v) are the most basic inputs to define a linear elastic material. In the next step, external load is applied over a selected region of the developed geometry.

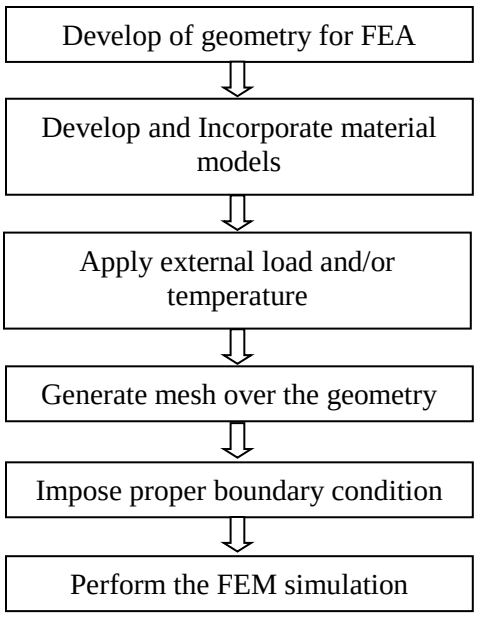

Figure 3: Flowchart of FEM modeling and validation

Temperature can also be applied in addition existing loading condition. After loading assignment, mesh is generated over the geometry to discretize the entire domain. Then, the FEA domain becomes a summation of a number of small elements as mentioned earlier. Local stiffness matrices are developed based on the element type and these matrices are assembled to generate the global stiffness matrix. Finally, boundary conditions, i.e., known force and deformation, are assigned on the selected nodes of a domain.

In this study, the FEM is developed in ABAQUS 6.10-EF-2 based on a pavement section on Milepost (MP) 141, Interstate 40 (I-40) near Albuquerque, New Mexico. This pavement section is instrumented with a number of strain gauges and pressure cells during reconstruction. The cross-section of this instrumented pavement section is shown in Figure 4. The pavement section consists of four major structural layers such as AC at the top, granular aggregate layer at the base, Process-Place and Compacted (PPC) aggregates in subbase, and engineered soil in subgrade. PPC layer is prepared by mixing of Reclaimed Asphalt Pavement (RAP) from surface as well as aggregate from base layer and then, compacting it in place. The elevation of strain gauges and pressure cells from the surface are shown. Total thickness of AC layer is 10.5 in. This AC layer consists of three lifts each with a thickness of 3.5 in. Thickness of the base is 6 in and the PPC layer is 8 in.

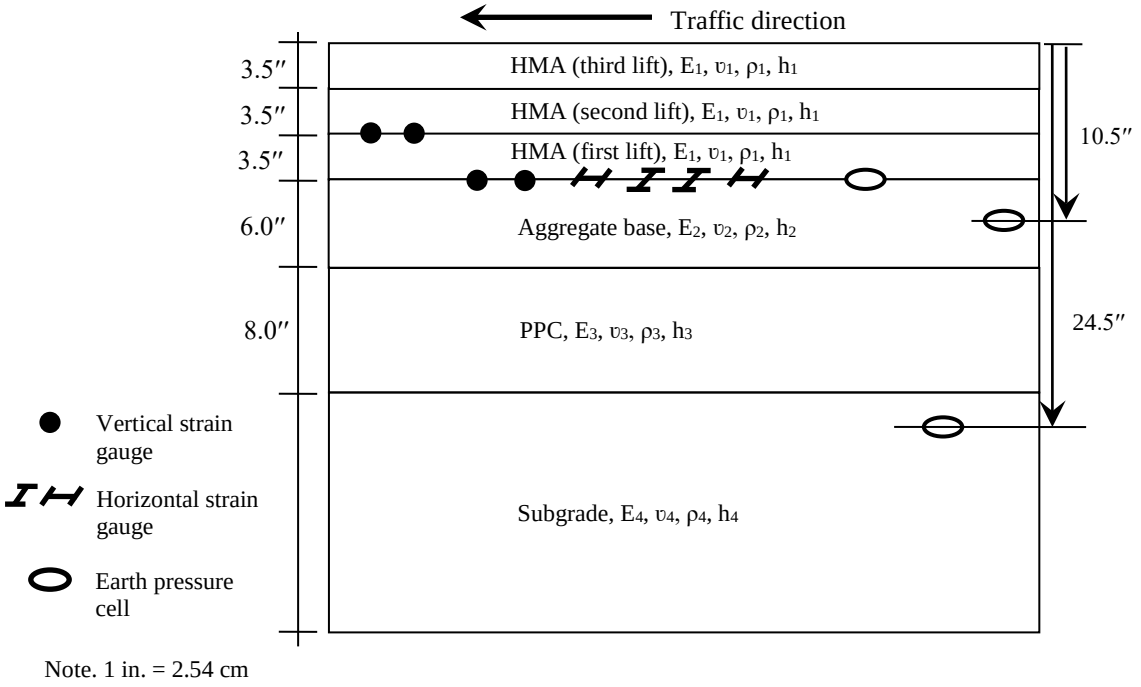

Figure 4: Instrumented Pavement Section (I-40, MP 141)

Plan view of the instrumentation section is shown in Figure 5. A total of fourteen horizontal asphalt strain gauges have been installed at the bottom of AC layer (Tarefder and Islam 2015). Seven Asphalt Strain Gauges (ASGs) have been placed along longitudinal direction, whereas seven other placed in the transverse direction of traffic. Four Earth Pressure Cells (EPCs) have been installed at different depths to measure the vertical stresses.

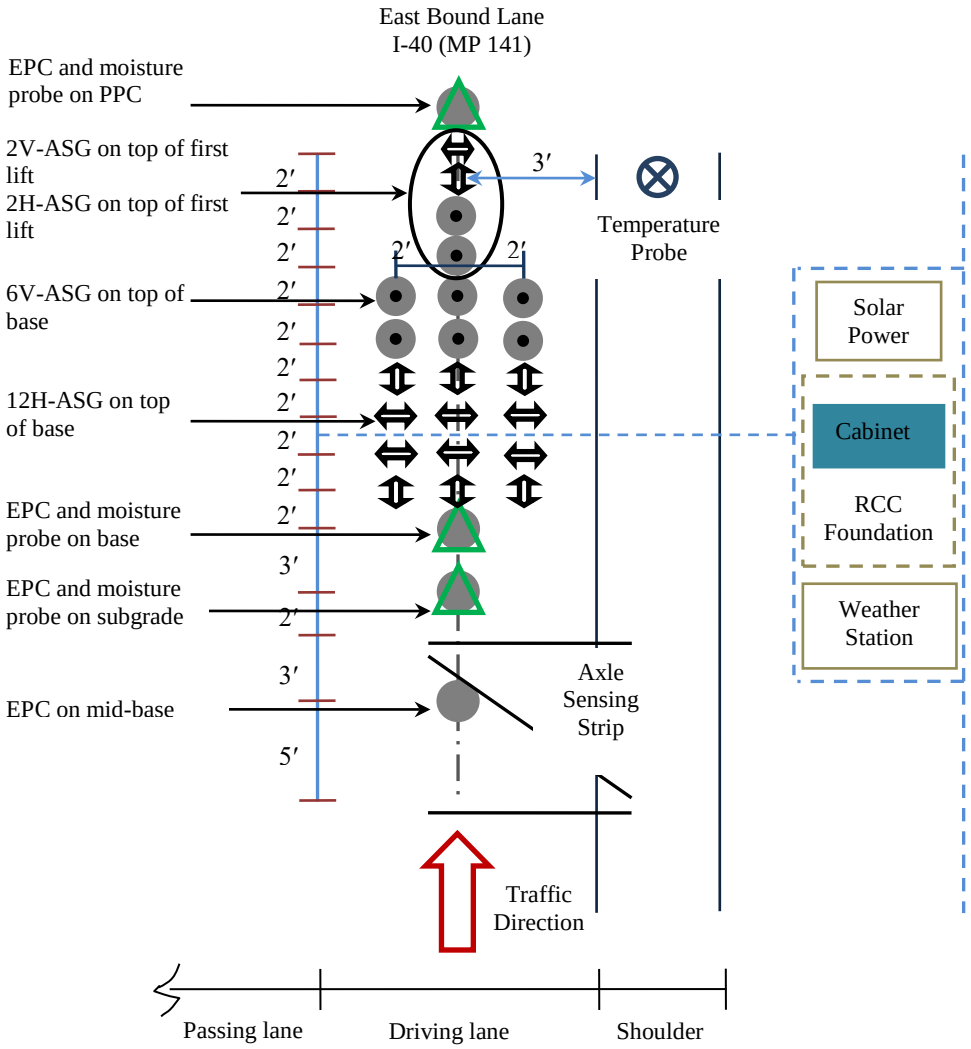

Note. 1 ft. = 30.48 cm

Figure 5: Plan View of Instrumented Pavement Section (I-40)

Model Geometry

A pavement section can be idealized by a 2D or 3D geometry in FEM (Abu-Farsakh et al. 2007, and Al-Qadi et al. 2010). FEM with 2D geometry is not compatible with different types of loading area. For an example, 2D axi-symmetric model is convenient to be loaded by circular plate, whereas 2D plane strain model is convenient for rectangular load. On the other hand, FEM with 3D geometry is convenient for any arbitrary shape of loading area.

The quarter cube geometry is selected to develop the model due to its two axes of symmetry (Figure 6). The depth and horizontal length of a model were selected to diminish the effect of stress near the boundary according to Duncan et al. (1968). The depth of the model is 50 times the loading radius, whereas the horizontal length is more than 12 times the loading radius. Wave reflection by the boundary is one of the major concerns in a dynamic analysis, which may occur due to the insufficient distance to the boundary (Petyt 1990). Therefore, the final dimensions,

i.e., length, width, and depth, of this entire model were selected to be 300 in. x 300 in. x 300 in. (7.62 m x 7.62 m x 7.62 m). The numbers of layers as well as thicknesses of every layer were assigned according to the instrumented section described earlier.

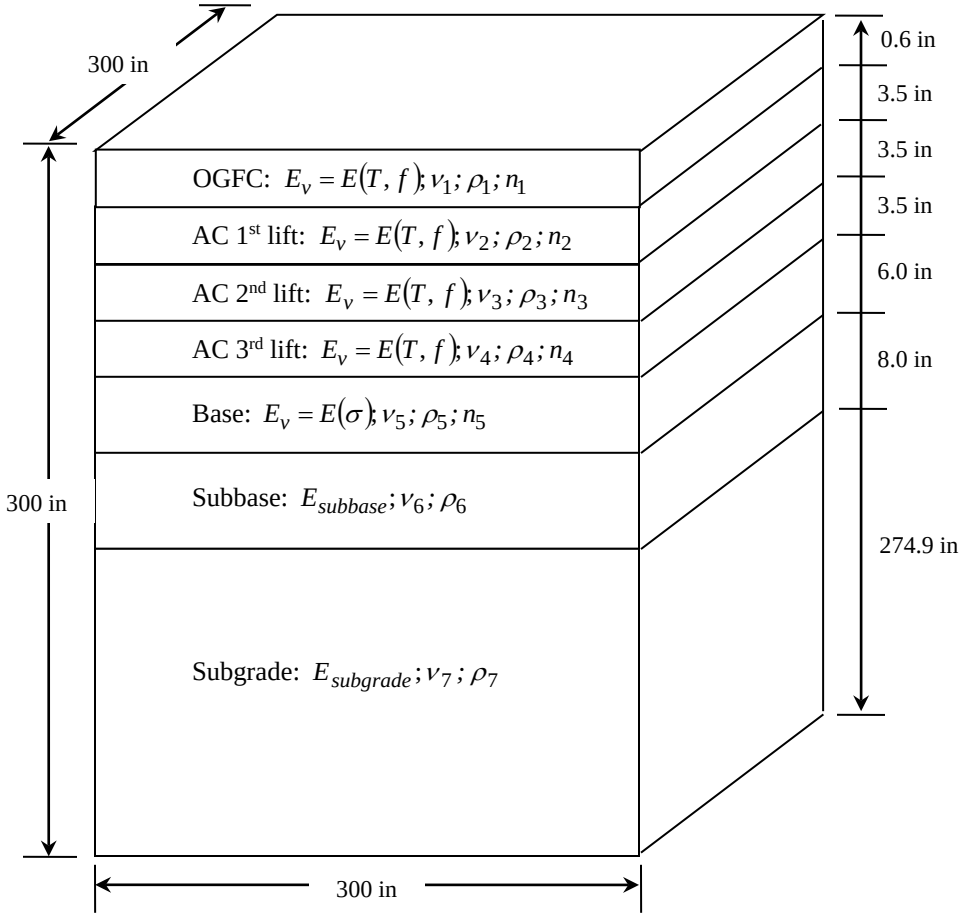

Figure 6: Multilayered structure of pavement section at MP 141, I-40

Boundary Condition

The so-called spring-dashpots are assigned at the boundaries in the two mutually orthogonal directions along both vertical and horizontal edge as shown in Figure 7 (Lysmer and Kuhlemeyer 1969, Novak et al. 1978, and Gazetas 1991). It is expected that stresses due to the repeated load will not be reflected back from the boundary due to the use of spring-dashpots.

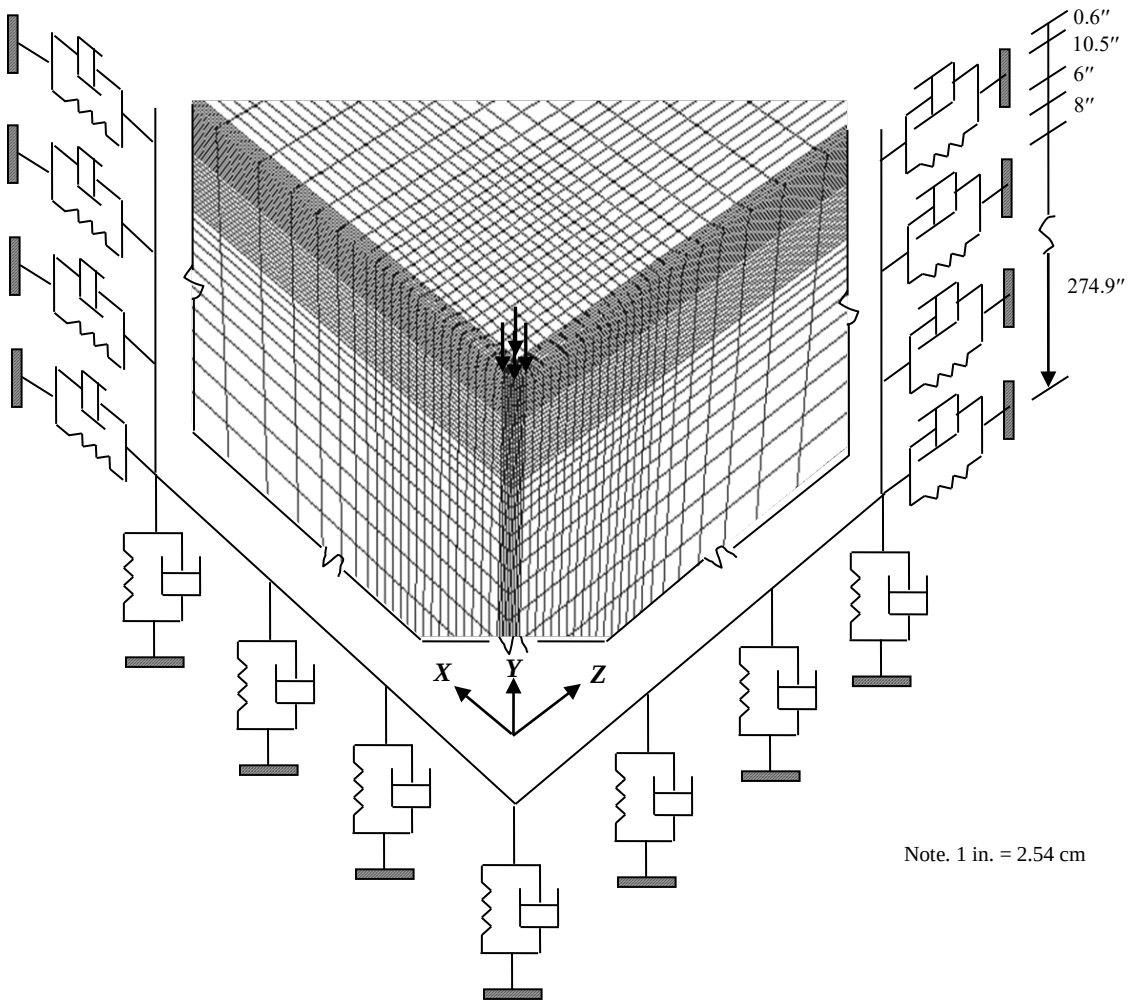

Figure 7: Boundary condition of the model

It is known that the pavement layer interfaces are typically partially-bonded which affects the pavement responses (Shahin et al. 1986, and Mehta 2007). Based on the visual inspection from coring, most of the layer interfaces were in good condition except the interface between the first and second lifts of the AC layer. Therefore, only this interface was considered as partially-bonded whereas the rest of the layer interfaces were considered as fully-bonded. The coulomb friction law was used to model the contact along the layer interfaces (Molinari et al. 2012). According to this law, $\tau = \mu\sigma_N$, where $\tau =$ shear stress, $\sigma_N =$ normal stress, and $\mu =$ friction coefficient. Friction coefficients required to define this contact model at different layer interfaces are collected from the literature (Romanoschi and Metcalf 2001). The friction coefficient along partially-bonded interfaces in AC is 0.7 and that along the other interfaces is 1.0 (fully-bonded).

Mesh Generation

An 8-noded brick element (C3D8) is used for the mesh generation. The size of the element during the mesh generation is selected after a number of trial analyses during a mesh-sensitivity analysis (Figure 8). The mesh-sensitivity analysis is performed by simulating the FEM for

varying sizes of elements. During the mesh-sensitivity analysis, material property is assumed based on Ahmed et al. (2013). The element size near the loading area is varied due to the influence of these elements on the stress gradient. In essence, a number of simulations were performed by reducing the depth of elements in AC layer from 89 mm (3.5 in.) to 13 mm (0.5 in.). In each of the simulations, vertical surface deflection is determined at the node that coincides with the center of the load. The effect of the element size variation on the vertical surface deflection shows that the deflection diminishes with gradual reduction of the depth of this element. The trend of vertical deflection with element depth variation begins to be constant from the simulation with the element depth of 18 mm (0.7 in.). Based on the consideration of accuracy, analysis time and memory storage for the dynamic simulations, the optimum depth of the smallest element is found to be 18 mm (0.7 in.). The largest dimension of this model is 1049.25 mm (41.97 in) at the bottom.

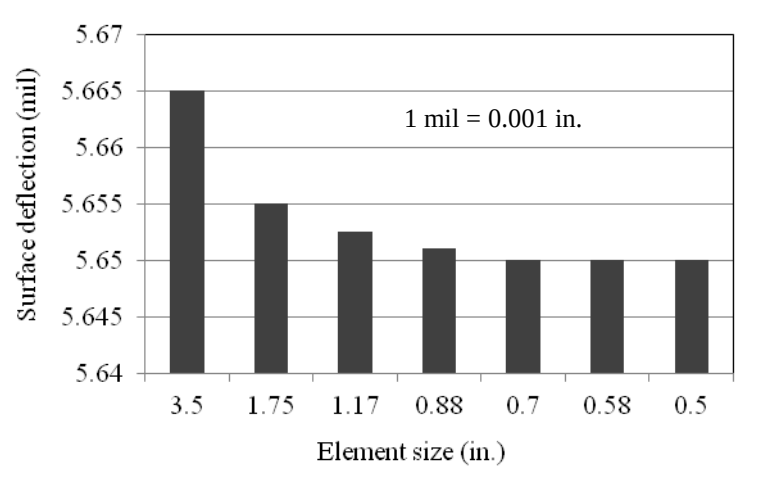

Figure 8: Mesh sensitivity analysis

Load

Researchers showed that tire contact stress is not uniform over a tire imprint area (Siddharthan et al. 2002, Al-Qadi and Wang 2009, and Roque et al. 2000). In this study, non-uniform vertical tire contact stresses over the tire imprint area are applied as the wheel load. Figure 9(a) shows the dimension of ribs of a single radial tire from the arrangement of a dual tire 275/80R22.5 as well as the distribution of vertical contact stress over the ribs based on the literatures (Al-Qadi and Wang 2009). The hot-inflated tire pressure is 104.4 psi (720 kPa). There are about five ribs in this tire. The ribs are numbered according to the similar stress magnitudes. Figure 9(b) shows the loading duration of the single tire at 96.5 km/hr (60 mph). The loading duration for each of the ribs is assumed to be the same and the duration is 0.03 second. In addition, the peak stresses of the ribs are assumed to be attained at the same time, i.e., 0.015 second.

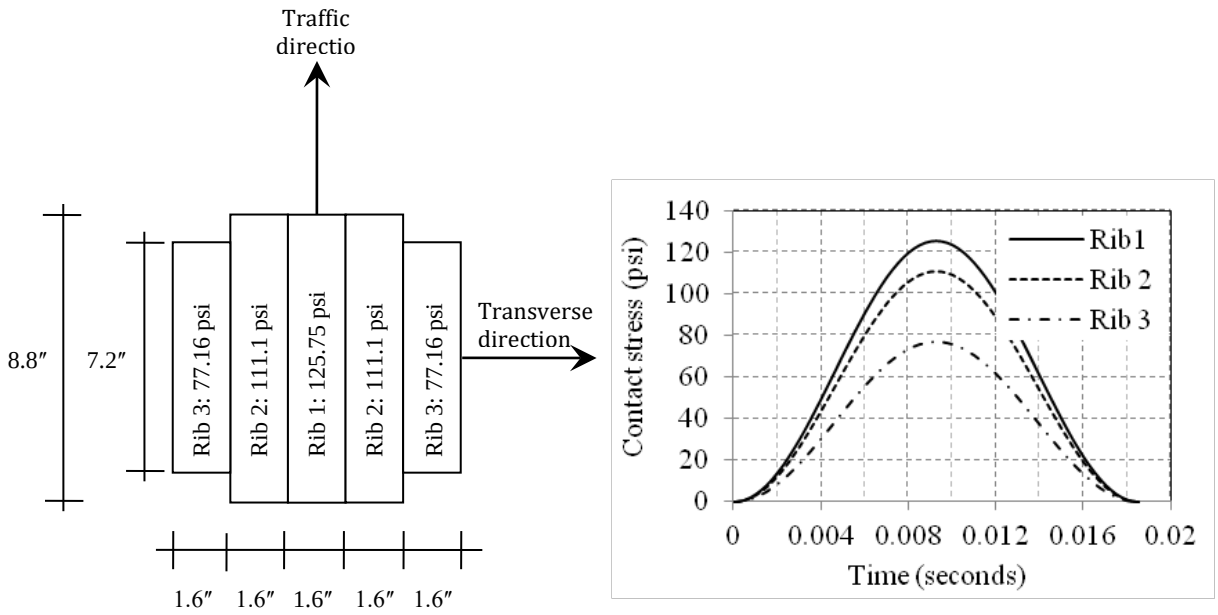

(a) Contact stress (b) Loading duration

Figure 9: Contact stress distribution and loading duration

Cross-Anisotropy

State of stresses, i.e., normal and shear stresses, on a 2-D rectangle element due to vertical load is shown in Figure 10. In a 3-D Cartesian reference system, there are total of nine stress components (σ_{ij}, $i, j = 1$, 2, and 3) on a cube element. The first subscript, *i*, denotes an axis which is perpendicular to a specific surface of stresses. The second subscript, *j*, denotes an axis which is along the stress direction. Among these components, three are normal stresses (σ_{ij} where $i = j$) and the rest are shear stresses (σ_{ij} where $i \neq j$). Strains (ε_{ij}) related to each of the earlier mentioned stresses are also shown in Figure 10.

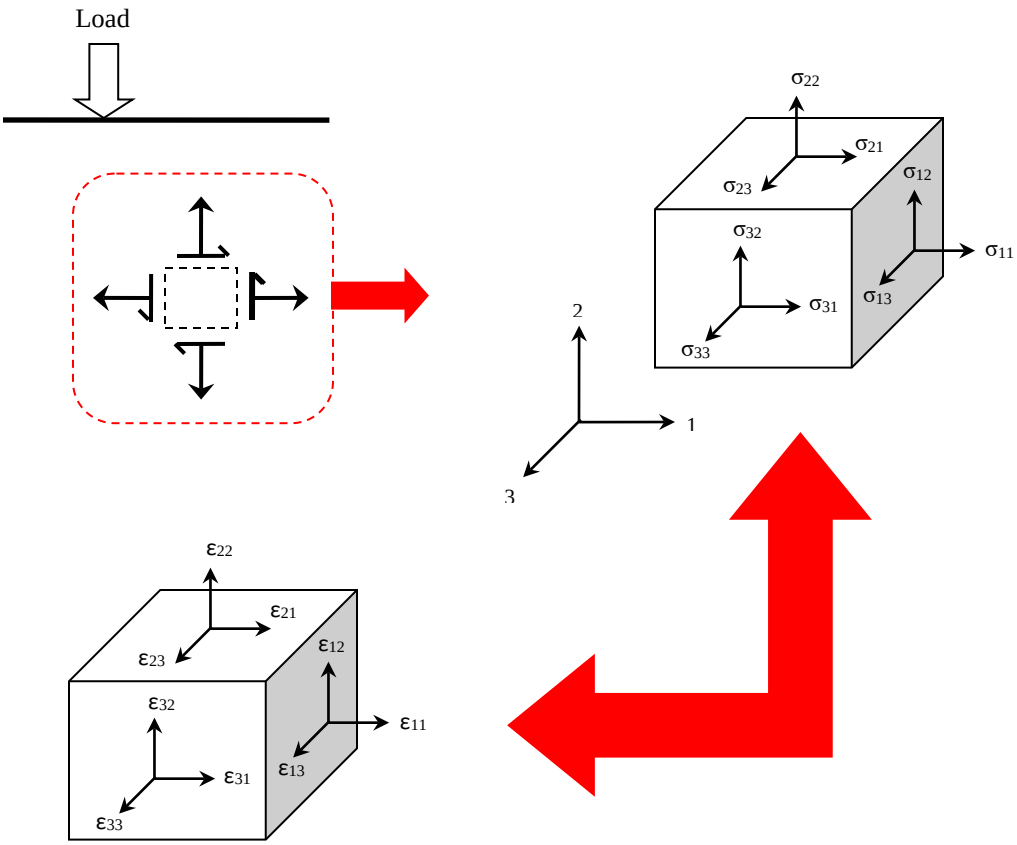

Figure 10: State of stresses

Stresses and strains are correlated by the Hooke's law (Sadd 2009). According to this law, stress is equal to product of strain and modulus of elasticity, i.e., $\sigma = E\varepsilon$, where $E =$ modulus of elasticity. This expression is a basic relationship between stress and strain. In case of the earlier mentioned state of stresses, the generalized form will be: $\sigma_{ij} = C_{ijkl}\varepsilon_{kl}$, where $C_{ijkl} =$ modulus of elasticity along different directions and $i, j, k, l = 1$, 2, and 3. This generalized form is expanded in a matrix form as shown in eqn. (2). It is observed that nine components of stresses are related to strains based on a total of 81 components of modulus of elasticity.

$$\begin{Bmatrix} \sigma_{11} \\ \sigma_{22} \\ \sigma_{33} \\ \sigma_{23} \\ \sigma_{31} \\ \sigma_{12} \\ \sigma_{32} \\ \sigma_{13} \\ \sigma_{21} \end{Bmatrix} = \begin{bmatrix} C_{1111} & C_{1122} & C_{1133} & C_{1123} & C_{1131} & C_{1112} & C_{1132} & C_{1113} & C_{1121} \\ C_{2211} & C_{2222} & C_{2233} & C_{2223} & C_{2231} & C_{2212} & C_{2232} & C_{2213} & C_{2221} \\ C_{3311} & C_{3322} & C_{3333} & C_{3323} & C_{3331} & C_{3312} & C_{3332} & C_{3313} & C_{3321} \\ C_{2311} & C_{2322} & C_{2333} & C_{2323} & C_{2331} & C_{2312} & C_{2332} & C_{2313} & C_{2321} \\ C_{3111} & C_{3122} & C_{3133} & C_{3123} & C_{3131} & C_{3112} & C_{3132} & C_{3113} & C_{3121} \\ C_{1211} & C_{1222} & C_{1233} & C_{1223} & C_{1231} & C_{1212} & C_{1232} & C_{1213} & C_{1221} \\ C_{3211} & C_{3222} & C_{3233} & C_{3223} & C_{3231} & C_{3212} & C_{3232} & C_{3213} & C_{3221} \\ C_{1311} & C_{1322} & C_{1333} & C_{1323} & C_{1331} & C_{1312} & C_{1332} & C_{1313} & C_{1321} \\ C_{2111} & C_{2122} & C_{2133} & C_{2123} & C_{2131} & C_{2112} & C_{2132} & C_{2113} & C_{2121} \end{bmatrix} \begin{Bmatrix} \varepsilon_{11} \\ \varepsilon_{22} \\ \varepsilon_{33} \\ \varepsilon_{23} \\ \varepsilon_{31} \\ \varepsilon_{12} \\ \varepsilon_{32} \\ \varepsilon_{13} \\ \varepsilon_{21} \end{Bmatrix} \quad (2)$$

There is symmetry in stress and strain tensor, i.e., $\sigma_{ij} = \sigma_{ji}$ and $\varepsilon_{kl} = \varepsilon_{lk}$, which reduces 81 components to 36. The reduced form of the eqn. (1) is shown in eqn. (3). Three normal stress components are: σ_i where $i = 1$, 2, and 3 whereas three shear stress components are: τ_i where $j = 4$, 5, and 6. In case of strains, ε_i where $i = 1$, 2, and 3 are normal and γ_i where $j = 4$, 5, and 6 are shear components. In addition, the C_{ijkl}-matrix reduces to C_{ij}-matrix which comprises 36 independent components.

$$\begin{Bmatrix} \sigma_1 \\ \sigma_2 \\ \sigma_3 \\ \tau_4 \\ \tau_5 \\ \tau_6 \end{Bmatrix} = \begin{bmatrix} C_{11} & C_{12} & C_{13} & C_{14} & C_{15} & C_{16} \\ C_{21} & C_{22} & C_{23} & C_{24} & C_{25} & C_{26} \\ C_{31} & C_{32} & C_{33} & C_{34} & C_{35} & C_{36} \\ C_{41} & C_{42} & C_{43} & C_{44} & C_{45} & C_{46} \\ C_{51} & C_{52} & C_{53} & C_{54} & C_{55} & C_{56} \\ C_{61} & C_{62} & C_{63} & C_{64} & C_{65} & C_{66} \end{bmatrix} \begin{Bmatrix} \varepsilon_1 \\ \varepsilon_2 \\ \varepsilon_3 \\ \gamma_4 \\ \gamma_5 \\ \gamma_6 \end{Bmatrix} \tag{3}$$

These 36 independent components are further reduced to 21 components due to energy based symmetry. The modified form of the eqn. (3) is shown in eqn. (4). Therefore, it can be said that 21 independent components are necessary to define an anisotropic material.

$$\begin{Bmatrix} \sigma_1 \\ \sigma_2 \\ \sigma_3 \\ \tau_4 \\ \tau_5 \\ \tau_6 \end{Bmatrix} = \begin{bmatrix} C_{11} & C_{12} & C_{13} & C_{14} & C_{15} & C_{16} \\ & C_{22} & C_{23} & C_{24} & C_{25} & C_{26} \\ & & C_{33} & C_{34} & C_{35} & C_{36} \\ & & & C_{44} & C_{45} & C_{46} \\ & & & & C_{55} & C_{56} \\ & & & & & C_{66} \end{bmatrix} \begin{Bmatrix} \varepsilon_1 \\ \varepsilon_2 \\ \varepsilon_3 \\ \gamma_4 \\ \gamma_5 \\ \gamma_6 \end{Bmatrix} \tag{4}$$

A material is orthotropic whenever it has three orthogonal axes of symmetry. Due to presence of these axes of symmetry, number of components in eqn. (4) will reduce to 9 independent components and the modified form is eqn. (5).

$$\begin{Bmatrix} \sigma_1 \\ \sigma_2 \\ \sigma_3 \\ \tau_4 \\ \tau_5 \\ \tau_6 \end{Bmatrix} = \begin{bmatrix} C_{11} & C_{12} & C_{13} & 0 & 0 & 0 \\ & C_{22} & C_{23} & 0 & 0 & 0 \\ & & C_{33} & 0 & 0 & 0 \\ & & & C_{44} & 0 & 0 \\ & & & & C_{55} & 0 \\ & & & & & C_{66} \end{bmatrix} \begin{Bmatrix} \varepsilon_1 \\ \varepsilon_2 \\ \varepsilon_3 \\ \gamma_4 \\ \gamma_5 \\ \gamma_6 \end{Bmatrix} \tag{5}$$

A material is called cross-anisotropic or transversely isotropic whenever modulus of elasticity along two orthogonal axes (on a plane) is same and differs from that along an axis normal to that plane, i.e., $E_2 = E_1 \neq E_3$. In this type of anisotropy, number of independent components is reduced to 5, i.e., $C_{11}, C_{22}, C_{12}, C_{13}, C_{44}$.

$$\begin{Bmatrix}\sigma_1\\ \sigma_2\\ \sigma_3\\ \tau_4\\ \tau_5\\ \tau_6\end{Bmatrix}=\begin{bmatrix}C_{11} & C_{12} & C_{13} & 0 & 0 & 0\\ & C_{22} & C_{12} & 0 & 0 & 0\\ & & C_{11} & 0 & 0 & 0\\ & & & C_{44} & 0 & 0\\ & & & & \frac{C_{11}-C_{12}}{2} & 0\\ & & & & & C_{44}\end{bmatrix}\begin{Bmatrix}\varepsilon_1\\ \varepsilon_2\\ \varepsilon_3\\ \gamma_4\\ \gamma_5\\ \gamma_6\end{Bmatrix} \tag{6}$$

If the axis-*1*, *2* and *3* (in Figure 1) is expressed as *v*, *h* and *v*-directions where '*h*' is horizontal and '*v*' is vertical, eqn. (6) will become eqn. (7). It is observed that eqn. (7) has 5 independent components, i.e., E_v, E_h, G_{vh}, ν_{vh} and ν_{hh}, which is true for cross-anisotropy or transverse isotropy. Therefore, during analysis, these five mechanical parameters need to be determined to assign material cross-anisotropy.

$$[D]=\frac{1}{[C]}=\begin{bmatrix}\frac{1}{E_h} & -\frac{\nu_{vh}}{E_v} & -\frac{\nu_{hh}}{E_h} & 0 & 0 & 0\\ & \frac{1}{E_v} & -\frac{\nu_{vh}}{E_v} & 0 & 0 & 0\\ & & \frac{1}{E_h} & 0 & 0 & 0\\ & & & \frac{1}{G_{vh}} & 0 & 0\\ & & & & \frac{2(1+\nu_{hh})}{E_h} & 0\\ & & & & & \frac{1}{G_{hv}}\end{bmatrix} \tag{7}$$

A material becomes isotropy whenever the *E* and ν -values are same in every direction.

Viscoelasticity

A viscoelastic material exhibits both elasticity and viscosity. Basic feature of an elastic material is to store energy whenever it is deformed due to an external load and release this energy completely upon removal of the load. In brief, there are zero deformation and energy dissipation after a complete cycle of loading-unloading. In case of viscosity, energy is continuously dissipated with none stored. In reality, a number of engineering materials including the AC stores and dissipates in varying degrees during a loading-unloading cycle.

In discussion under the earlier section, it is mentioned that stress (σ) is equal to product of the modulus of elasticity (E) and strain (ε). The E-value can be determined from the slope of a stress-strain variation of a linear elastic material (see Figure 11(a)). Mechanical behavior of a linear elastic material can be expressed by a spring which shows instantaneous response during both loading and unloading. In case of a viscous material, energy dissipates due to resistance to flow or deformation and stress is equal to product of viscosity (η) and strain variation over time ($\dot{\varepsilon}$). Mechanical behavior of a viscous material can be expressed by a dashpot (see Figure 11(b)).

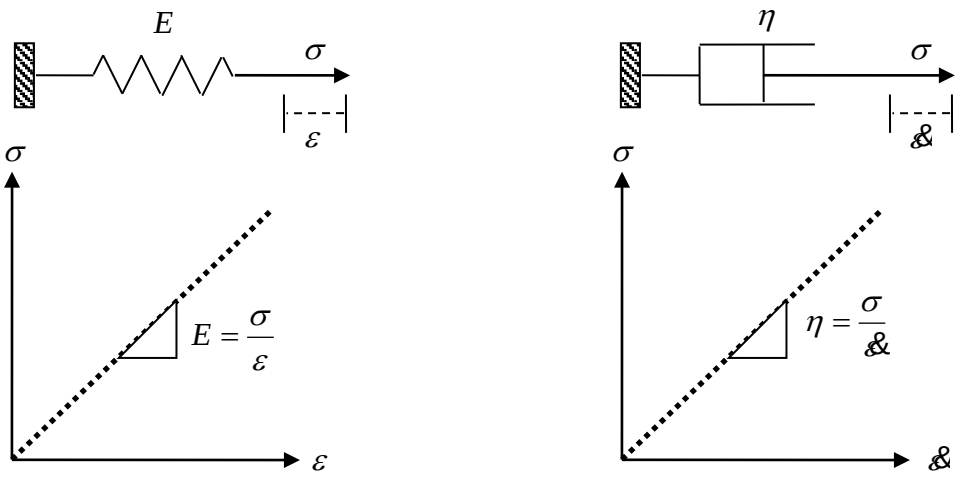

(a) Elasticity (b) Viscosity

Figure 11: Elasticity and viscosity

The above mentioned discussion indicates that mechanical behavior of a viscoelastic material can be expressed as combinations of spring and dashpot. Many different combinations can be used for this purpose. There are two basic mechanical models available for viscoelasticity and these are: Maxwell and Kelvin models respectively (Huang 2004).

Maxwell Model - It is a combination of a spring and a dashpot in series (Figure 12). Let, this model is subjected to an instantaneous strain which is constant over a certain span of time, i.e., $\varepsilon(t) = \varepsilon$. Total strain is summation of strains in spring (ε_s) and dashpot (ε_d) as below:

$$\varepsilon = \varepsilon_s + \varepsilon_d = \frac{\sigma}{E} + \frac{\sigma t}{\eta} = \frac{\sigma}{E}\left(1 + \frac{t}{T_{relax}}\right) \tag{8}$$

where T_{relax} = relaxation time = η/E. Figure 3 shows stress gradually decreases over time due constant strain. This behavior is known as relaxation. Eqn. (8) can be re-written as follows:

$$\frac{\partial \varepsilon}{\partial t} = \frac{1}{E}\frac{\partial \sigma}{\partial t} + \frac{\sigma}{\eta} \Rightarrow 0 = \frac{1}{E}\frac{\partial \sigma}{\partial t} + \frac{\sigma}{\eta} \Rightarrow -\frac{1}{E}\frac{\partial \sigma}{\partial t} = \frac{\sigma}{\eta} \Rightarrow -\frac{1}{E}\int_{\sigma_0}^{\sigma}\frac{d\sigma}{\sigma} = \frac{1}{\eta}\int_0^t dt \Rightarrow \sigma = \sigma_0 e^{-tE/\eta} \tag{9}$$

Special cases:

(a) $t = 0;\ \sigma = \sigma_0$

(b) $t = \infty;\ \sigma = 0$

(c) $t = T_{relax};\ \sigma = 0.368\sigma_0$

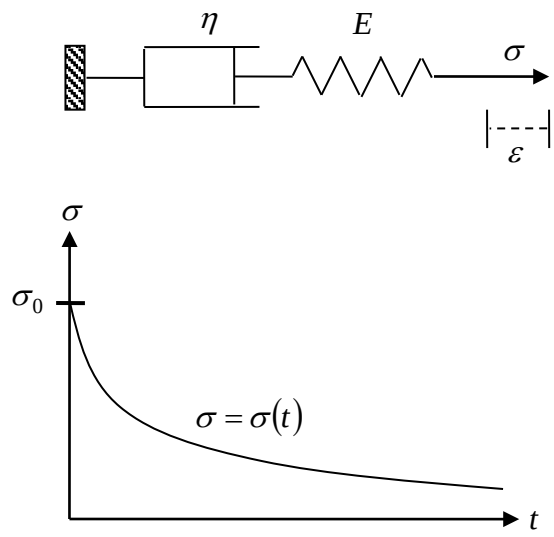

Figure 12: Maxwell model

Kelvin Model - It is a combination of a spring and a dashpot in parallel (Figure 13). Let, this model is subjected to an instantaneous stress which is constant over a certain span of time, i.e., $\sigma(t)=\sigma$. Total stress is summation of stresses in spring (ε_s) and dashpot (ε_d) as below:

$$\sigma = \sigma_s + \sigma_d = E\varepsilon + \eta\frac{\partial\varepsilon}{\partial t} \tag{10}$$

$$\int_0^{\varepsilon}\frac{d\varepsilon}{\sigma - E\varepsilon} = \int_0^{t}\frac{dt}{\eta} \Rightarrow -\frac{1}{E}\ln\left(\frac{\sigma - E\varepsilon}{\sigma}\right) = \frac{t}{\eta} \Rightarrow \varepsilon = \frac{\sigma}{E}\left(1 - e^{-tE/\eta}\right) \Rightarrow \varepsilon = \varepsilon_0\left(1 - e^{-t/T_{retard}}\right) \tag{11}$$

where T_{retard} = retardation time = η/E . Figure 12 shows strain gradually increases over time due constant stress. This behavior is known as retardation.

Special cases:
(a) $t=0;\ \varepsilon=0$
(b) $t=\infty;\ \varepsilon=\varepsilon_0$
(c) $t=T_{retard};\ \varepsilon=0.368\varepsilon_0$

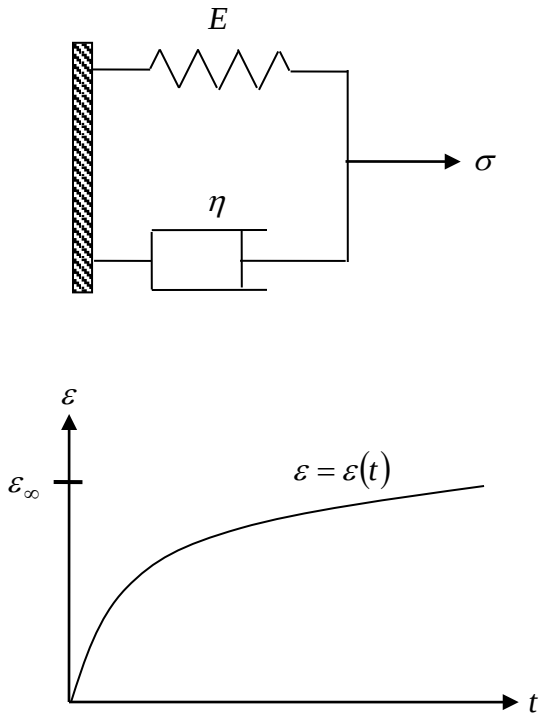

Figure 13: Kelvin model

Generalized Maxwell Model (GMM) - It is a model which includes *n*-number of Maxwell models/elements in parallel with a constant spring as shown in Figure 14 (Mase and Mase 1999, and Buechlar 2012). The spring has an elastic modulus (E_∞) which is known as long term modulus. The Maxwell elements have both modulus (E_i) and viscosity (η_i) and each of these elements has individual relaxation time ($\tau_i = \eta_i / E_i$). Stress calculation based on this model will be described under this subsection. Prior to the derivation, derivative of the eqn. (8) respect to time is as follows:

$$\dot{\varepsilon} = \dot{\varepsilon}_s + \dot{\varepsilon}_d = \frac{\dot{\sigma}}{E} + \frac{\sigma}{\eta} \tag{12}$$

It is mentioned earlier that the relaxation time is ratio of viscosity and modulus of elasticity for single Maxwell element. Here, it is denoted by τ and $\tau = \eta / E$. Now, eqn. (12) becomes:

$$\dot{\varepsilon} = E\dot{\varepsilon} - \frac{\sigma}{\tau} \tag{13}$$

Laplace transformation of eqn. (13) leads to:

$$s\sigma(s) = sE\varepsilon(s) - \frac{\sigma(s)}{\tau} \Rightarrow \sigma(s) = \frac{sE}{s + \frac{1}{\tau}}\varepsilon(s) \tag{14}$$

Now, the inverse Laplace transform of eqn. (14) back to time domain yields the following form:

$$\sigma(t) = \int_{t'=0}^{t'=t} E e^{\left[-(t-t')/\tau\right]} dt' \tag{15}$$

It is the most basic integral form of the Maxwell model for stress-strain calculation. This equation is used later to derive general integral form for the GMM.

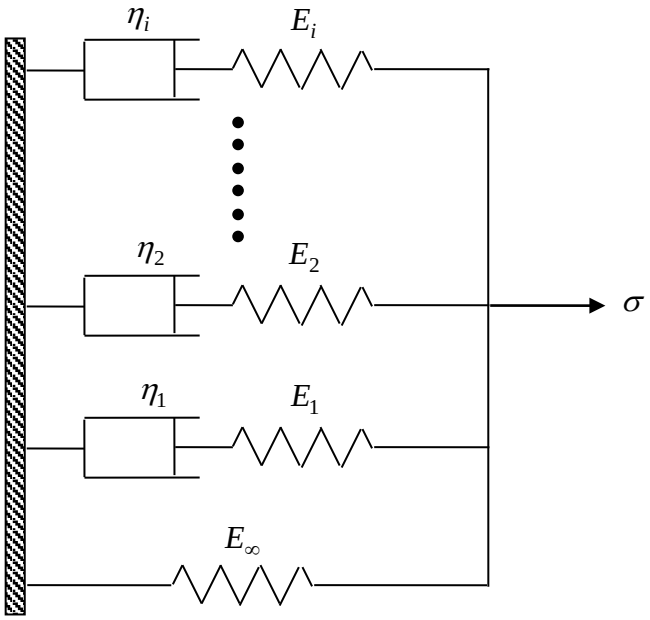

Figure 14: Generalized Maxwell Model

Summing up the spring and the Maxwell elements using the eqn. (15), the generalized form is as below:

$$\sigma(s) = \left(E_\infty + \sum_{i=1}^{n} \frac{sE_i}{s + 1/\tau_i} \right) \varepsilon(s) \tag{16}$$

Inverse Laplace transformation of eqn. (16) leads to:

$$\sigma(t) = \int_{t'=0}^{t'=t} \left\{ E_\infty + \sum_{i=1}^{n} E_i e^{\left[-(t-t')/\tau_i\right]} \right\} dt' \tag{17}$$

Simplest form of eqn. (17) is as follows:

$$\sigma(t) = \int_{t'=0}^{t'=t} E(t-t') dt' \tag{18}$$

where $E(t) = E_\infty + \sum_{i=1}^{n} E_i e^{\left(-t/\tau_i\right)}$ and this can be further modified to:

$$E(t) = E_0\left[1 - \sum_{i=1}^{n} e_i\left\{1 - \exp^{\left(-t/\tau_i\right)}\right\}\right] \tag{19}$$

In this study, eqn. (19) will be adopted to assign AC viscoelasticity to the dynamic FEM of pavement. This equation is typically known as Prony series.

Depth-temperature Variation in AC

It is also known that pavement temperature varies over the depth which indicates that the AC modulus should also vary over the depth due to its temperature dependency. This temperature dependency of AC modulus is incorporated based on an assumption of linear depth-temperature variation. Therefore, the equation for the temperature variations is as follows:

$$T_z = T_{surface} - \frac{\left(T_{surafce} - T_{bottom}\right) \times z}{D} \tag{20}$$

where T_z = temperature of the AC at depth, z (ºC), $T_{surface}$ = surface temperature (ºC), T_{bottom} = temperature at bottom of the AC layer (ºC), and D = thickness of the AC layer (in.). The surface and bottom temperatures are measured by the temperature probe installed at specific depths of the AC layer. Figure 15 shows the qualitative trend of AC modulus over the depth due to incorporation of this temperature dependency. In most of the time, surface and bottom temperatures are not the same. Therefore, AC modulus at the surface and bottom will also be different.

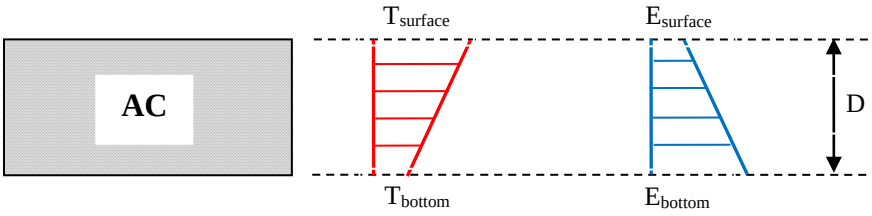

Figure 15: Depth-temperature variation in AC layer

The temperature dependency of AC moduli for both vertical and horizontal directions is incorporated as follows (Appea 2003):

$$\frac{E_{v(T=21°C)}}{E_v(z)} = e^{-0.0342(21-T)} \tag{21}$$

$$\frac{E_{h(T=21°C)}}{E_h(z)} = e^{-0.0342(21-T)} \tag{22}$$

where $E_{v(T=21°C)}, E_{h(T=21°C)}$ = vertical and horizontal AC modulus at 21 °C respectively, $E_{v(z)}, E_{h(z)}$ = vertical and horizontal AC modulus at a depth 'z' respectively, and T = temperature at depth 'z'. A subroutine is developed in FORTRAN to implement the temperature dependent and cross-anisotropic viscoelastic model of the AC layer. Later, this subroutine is integrated to the dynamic FEM in ABAQUS using the User Defined Material (UMAT) interface.

TASK 2: LABORATORY TESTING OF MATERIAL INPUTS

Quantifying Cross-Anisotropy and Viscoelasticity

Cores are collected from the same instrumented pavement section using a portable 6 in diameter core drill bit (see Figure 16). The AC layer has three lifts each with a similar thickness of 3.5 in. During the coring, it is observed that the top layer interface is partially-bonded, whereas the bottom layer interface is fully-bonded.

Figure 16: Extraction of field-compacted AC core

Both vertical and horizontal AC cores are required for laboratory tests, such as dynamic modulus test, to determine the viscoelastic and cross-anisotropic parameters. The dynamic modulus tests require specific dimension for test specimen. The criteria for the dimension are as below:

- Gauge length should be equal or greater than 3 times the nominal aggregate size
- Difference between the end of a LVDT and edge of a test specimen should be fairly 1 inch to avoid possible presence of stress-concentration
- Any interface, such as partially-bonded interface, should be outside the gauge length

Figure 17 shows the preparation of vertical AC test specimen. Height and diameter of this core are 4.5 and 3 inch respectively.

Figure 17: Preparation of vertical test specimen for laboratory tests

Figure 18 shows the sample preparation for horizontal AC core. The field-compacted core was first cut on two sides by a saw to place it inside a casing of the core drill. A 3 in diameter core drill is used to extract the core. The 3 in diameter extracted core is again cut at the two ends to make 4.5 in height test specimen with smooth surfaces.

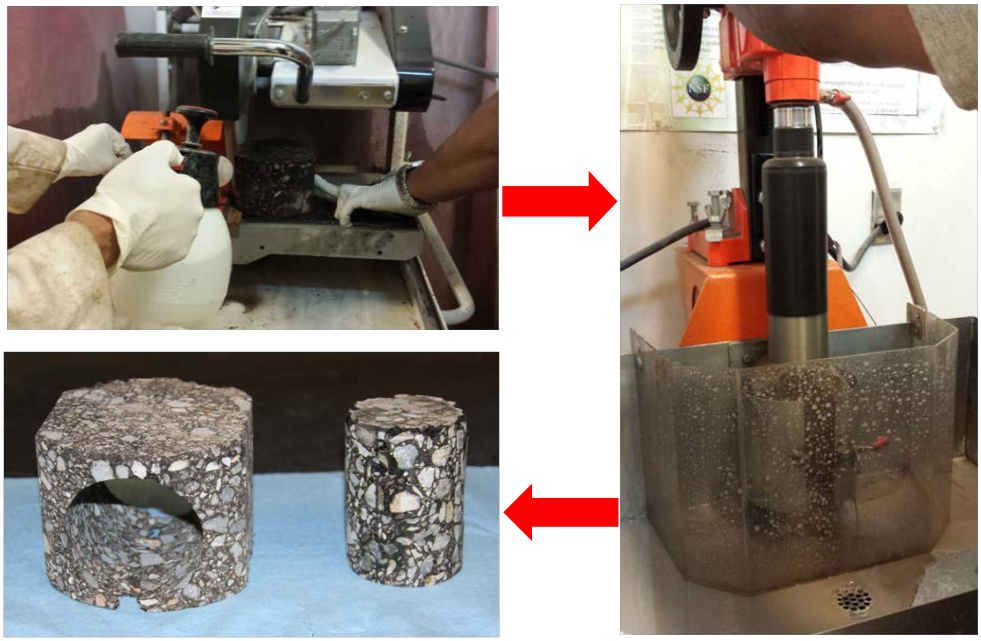

Figure 18: Preparation of horizontal test specimen for laboratory tests

Dynamic modulus tests were conducted according to AASHTO T 342-11 (2015). Figure 19 shows the test setup where the test specimen is subjected a repeated uniaxial load. Three LVDTs are attached vertically to the specimen measure the deformation under the repeated load. According to the guideline, the tests are conducted at different frequencies and temperatures. These frequencies are: 0.1, 0.5, 1, 5, 10 and 25 Hz and temperatures are: -10, 4, 21, 37, and 54 °C.

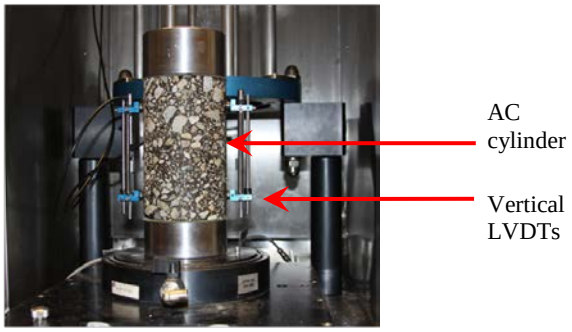

Figure 19: Dynamic modulus test

Dynamic modulus of the vertical AC core at pre-selected frequencies and temperatures are shown in Figure 20(a). Based on these values, a dynamic modulus master curve is generated using the Time-Temperature Superposition (TTSP). The master curve is shown in Figure 20(b). Relaxation modulus values are determined from the dynamic modulus master curve which is shown in Figure 19(c).

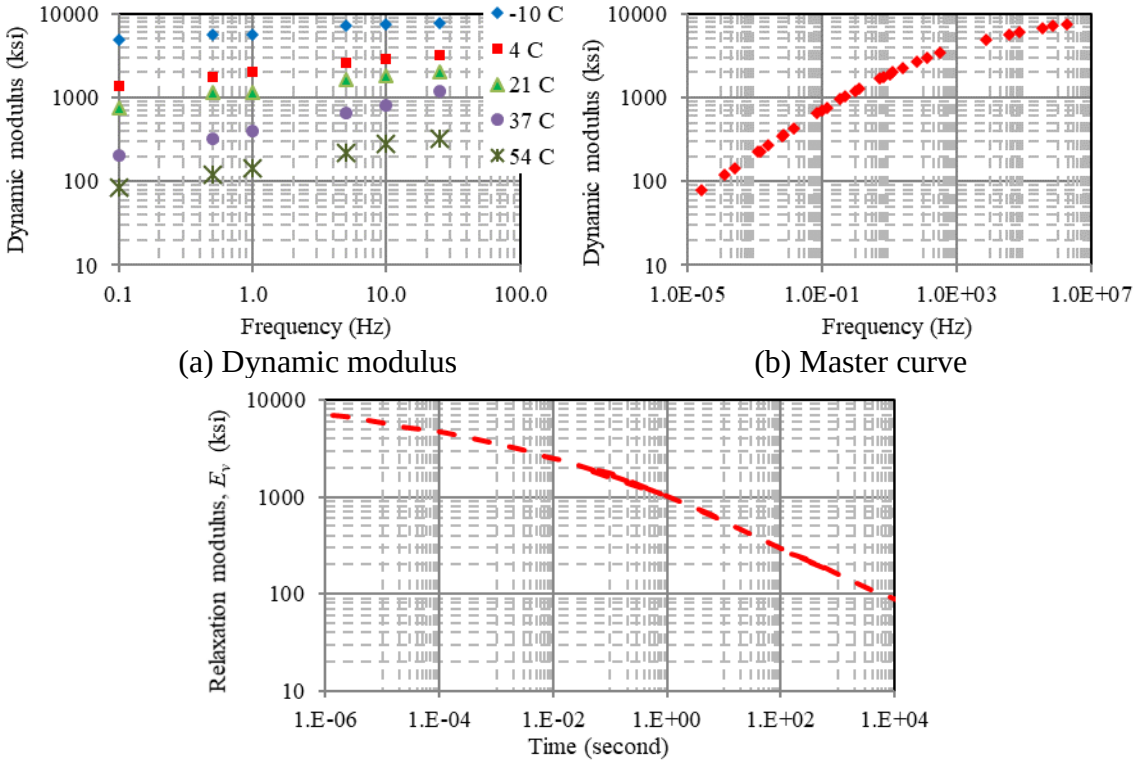

(a) Dynamic modulus

(b) Master curve

(c) Relaxation modulus

Figure 20: Dynamic and relaxation modulus of vertical AC core

Dynamic modulus of the horizontal AC core at pre-selected frequencies and temperatures are shown in Figure 21(a). Based on these values, a dynamic modulus master curve is generated using the TTSP. The master curve is shown in Figure 21(b). Relaxation modulus values are determined from the dynamic modulus master curve which is shown in Figure 21(c).

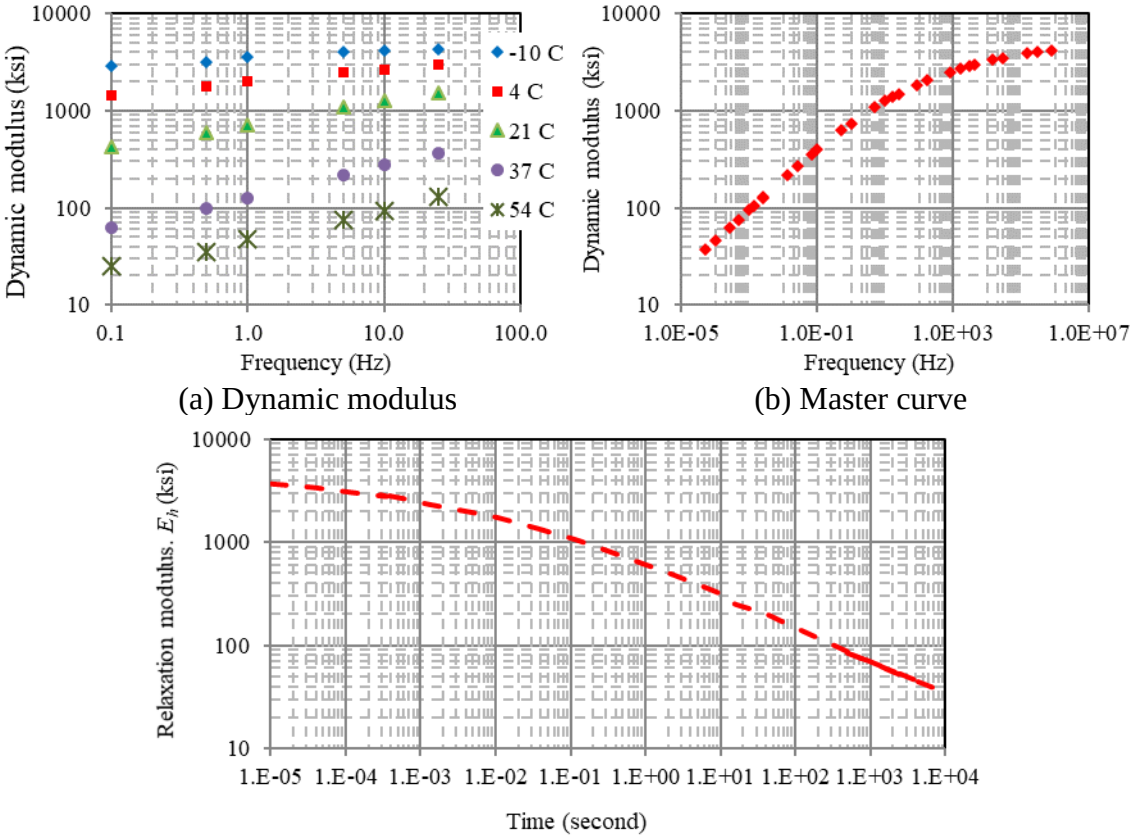

(a) Dynamic modulus (b) Master curve

(c) Relaxation modulus

Figure 21: Dynamic and relaxation modulus of horizontal AC core

Based on the dynamic modulus test results, parameters of required for the eqn. (19) are determined using an optimization technique in MATLAB. These are summarized in Table 1. A total of six spring-dashpot(s) are used during the optimization. Parameters in the second and third columns are for the vertical AC core whereas those in the fourth and fifth columns are for the horizontal AC core. Instantaneous moduli along vertical and horizontal directions are 7037 and 3795 ksi respectively. These Prony series parameters are used in the material model developed in the FORTRAN.

Table 1: Prony Series Coefficient (vertical & horizontal AC cores)

i	$e_{v,i}$	$\tau_{v,i}$	$e_{h,i}$	$\tau_{h,i}$
1	0.277	1.04E-05	0.292	0.001
2	0.2	0.018	0.2	0.056
3	0.15	0.0011	0.15	15.64
4	0.13	0.00019	0.19	0.0001
5	0.13	0.68	0.1	0.61
6	0.09	22.99	0.054	0.02

Unbound Layers: Stress-Dependency

In a typical pavement section, aggregate and fine soil are known as unbound materials due to very little to no cohesion. In the past, it was reported these materials are nonlinear elastic and stress-dependent (Hicks and Monismith 1971, and Uzan 1985). In case of nonlinear elasticity, material undergoes deformation during loading and regains its original shape after removal of load similar to linear elasticity. However, the entire trend is nonlinear instead of linear as observed in linear elasticity (Figure 22(a)). Generally, an unbound material exhibits very little to no stiffness without confining pressure, i.e., geo-static pressure. In presence of confining pressure and deviator stress, i.e., imposed traffic stress, stiffness may vary. A material exhibits stress-hardening whenever the stiffness increases with increase in the earlier mentioned stresses (Figure 22(b)). This behavior is observed mostly in granular aggregates.

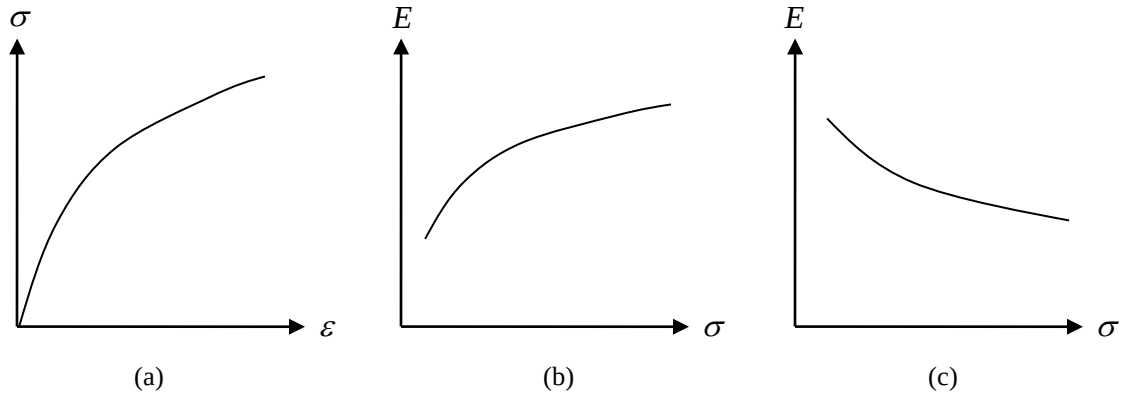

Figure 22: Nonlinearity of unbound layer materials

In some other materials, stiffness decreases as the stress increases (Figure 22(c)). This behavior is known as stress-softening and it is observed in fine soils. In reality, a number of unbound materials show both of stress-hardening and/or softening.

The stress-dependency of unbound material are commonly characterized by resilient modulus tests in triaxial chamber. During a test, resilient modulus (M_R), i.e., ratio of axial stress (σ_a) and resilient strain (ε_r), is determined at varying confining pressure (σ_c) and deviator stress (σ_d) and the details will be discussed in the following section. In the pavement engineering arena, this issue was first addressed by Hicks and Monismith (1971). It was observed that M_R of unbound

material is mainly dependent on bulk stress, i.e., $\theta = \sigma_a + 2\sigma_r$ where σ_r = radial stress (Figure 23). In this study, the $K-\theta$ model was proposed to correlate M_R and θ of unbound materials. This model is as follows:

$$M_R = K(\theta)^n \tag{23}$$

where K, n = regression coefficients. This model is good for coarse aggregate where the normal stresses at particle contact interfaces are dominant. However, in case of fine soil, this model has a shortcoming since it fails to adequately distinguish the effect of shear behavior.

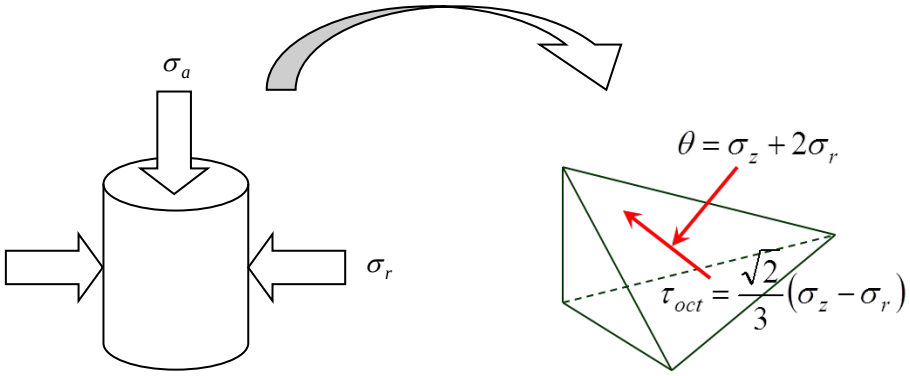

Figure 23: State of stresses in unbound material under resilient modulus test

Later, Uzan (1985) modified this model to address the shear behavior. The modified model is as below:

$$M_R = k_1(\theta)^{k_2}(\sigma_d)^{k_3} \tag{24}$$

where σ_d = deviatoric stress $(= \sigma_a - \sigma_r)$, and k_1, k_2, k_3 = regression coefficients. It is known that the normal and shear stresses, i.e., θ and τ_{oct} = octahedral shear stress, along octahedral plane are greater than any other stresses. In addition, these stresses are function of all the principal stresses. Therefore, it is more reasonable to use these specific stresses to incorporate the stress-dependency. Later, this model was also modified by replacing σ_d by τ_{oct}. The modified model is known as universal octahedral shear stress model (Wiczack and Uzan 1988). This model is as follows:

$$M_R = k_1 p_a \left(\frac{\theta}{p_a}\right)^{k_2} \left(\frac{\tau_{oct}}{p_a}\right)^{k_3} \tag{25}$$

where p_a = atmospheric pressure. In eqn. (25), M_R will be surprisingly small if τ_{oct} tends to very small even though θ is not small. Therefore, this model was also modified which is known as Mechanistic Empirical Pavement Design Guide (MEPDG) model for unbound layers (Witczack and El-Basyouny 2004). This model is as follows:

$$M_R = k_1 p_a \left(\frac{\theta}{p_a} \right)^{k_2} \left(\frac{\tau_{oct}}{p_a} + 1 \right)^{k_3} \quad (26)$$

This model can be used for different types of unbound materials which may exhibit only stress-hardening and/or softening.

Quantifying Stress-Dependency

Stress-dependencies of unbound materials from base and subbase layers were determined based on the resilient modulus test. This test was conducted according to the AASHTO T307-99 (2003). Figure 24 shows that a cylinder test specimen of unbound material with 4 in. diameter and 8 in. height. The reason for selecting this dimension is that the Nominal Maximum Aggregate Size (NMAS) of both base and subbase aggregates is not above 0.75 inch. The specimen was kept inside a triaxial cell to apply confining pressure by compressed air. A load cell (capacity of 5000 lbs) was used to apply repeated axial load. External LVDTs were used to measure the vertical deformation under this repeated load.

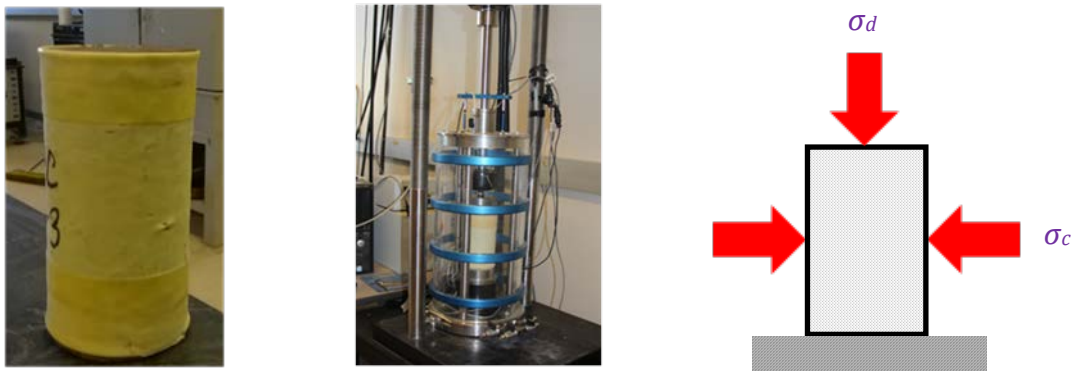

(a) Test specimen (b) Resilient modulus (c) State of stresses

Figure 24: Laboratory resilient modulus tests

During the test, the test sample was subjected to a confined pressure (σ_c), i.e., cell pressure applied through compressed air. Once the sample was confined to cell pressure, the deviatoric pressure (σ_d) was applied on the flat surface of the sample along the vertical direction by the load cell. The 10% of this deviatoric pressure was applied in static mode and the rest 90% was applied in cyclic mode. The sample was subjected to a total of 5000 loading cycles. Resilient modulus (M_r) was calculated using the deviatoric stress (σ_d) and the average irrecoverable strain (ε_r) from the last five cycles as follows:

$$M_r = \frac{\sigma_d}{\varepsilon_r} \quad (26)$$

A stress-sequence as defined by the AASHTO T307-99 (2003), for granular aggregates, was followed during the test. Resilient modulus (M_r) values were determined at each of these stress-

sequences. Later, two stress parameters such as bulk (θ) and octahedral shear (τ_{oct}) stresses are determined from the state of stresses using the following relationships:

$$\theta = \sigma_1 + \sigma_2 + \sigma_3 = \sigma_d + 2\sigma_c \tag{27}$$

$$\tau_{oct} = \frac{1}{3}\sqrt{(\sigma_1 - \sigma_2)^2 + (\sigma_2 - \sigma_3)^2 + (\sigma_1 - \sigma_3)^2} \tag{28}$$

where, $\sigma_1, \sigma_2, \sigma_3$ = principal stresses along three mutually orthogonal directions. In this study, σ_2 = major principal stress along vertical direction $(= \sigma_c + \sigma_d)$, and $\sigma_1 = \sigma_3$ = principal stresses along horizontal plane $(= \sigma_c)$. Therefore, eqn. (28) can be rewritten as follows:

$$\tau_{oct} = \frac{\sqrt{2}}{3}\sigma_d \tag{29}$$

Resilient modulus values of both base and subbase aggregates are plotted against bulk and octahedral shear stress respectively (see Figure 25(a) and (b)). In case of base layer, resilient modulus increases with increase in both bulk and octahedral shear stress. From the initial to the final stress sequence resilient modulus increases by about 100 ksi. In case of subbase, resilient modulus also increases with these states of stresses. However, this change is small compared to base layer. Based on the overall observation, both of these unbound layers are stress-dependent.

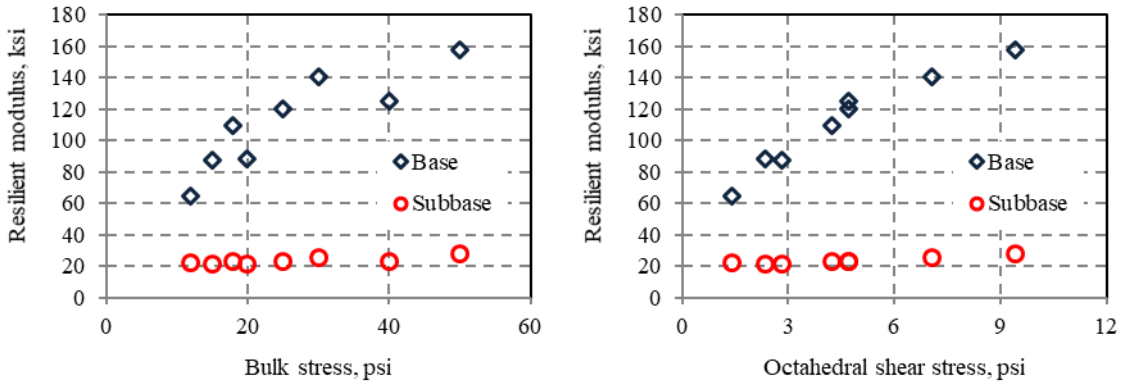

(a) Bulk stress variation (b) Octahedral shear stress variation

Figure 25: Laboratory resilient modulus tests

Stress-dependencies of both base and subbase layers need to be incorporated to the pavement model. The generalized model as adopted in the newly developed MEPDG, i.e., eqn. (4) is used in this study to incorporate base and subbase stress-dependency. Coefficients, i.e., k_1, k_2, k_3, of the eqn. (4) are determined using a nonlinear regression analysis, and these are summarized in Table 2. The base shows only stress-hardening whereas the subbase shows both stress-hardening and softening.

Table 2: Summary of regression coefficients

Layer	k_1	k_2	k_3
Base	5385	0.15	0.75
Subbase	1722	0.17	-0.27

Integrating Stress-Dependency

A FORTRAN subroutine is developed to implement the stress-dependent and nonlinear elastic unbound material model in FEM and the flow chart is shown in Figure 26. At the beginning, an initial stiffness or tangent modulus is assigned based on the trend of resilient modulus variation at varying stress. Strains are calculated using this initial tangent modulus under a load/stress through the FEM, i.e., ABAQUS 6.10-EF-2. Stresses at different points over a continuum are then determined as 'Output Stresses' at an analysis/time step from these strains incorporating the tangent modulus. Resilient modulus is then determined from these stresses using eqn. (26), and it is fed back to the main module of the FEM as the tangent modulus for further determination of strain. The entire process is repeated till the end of analysis duration.

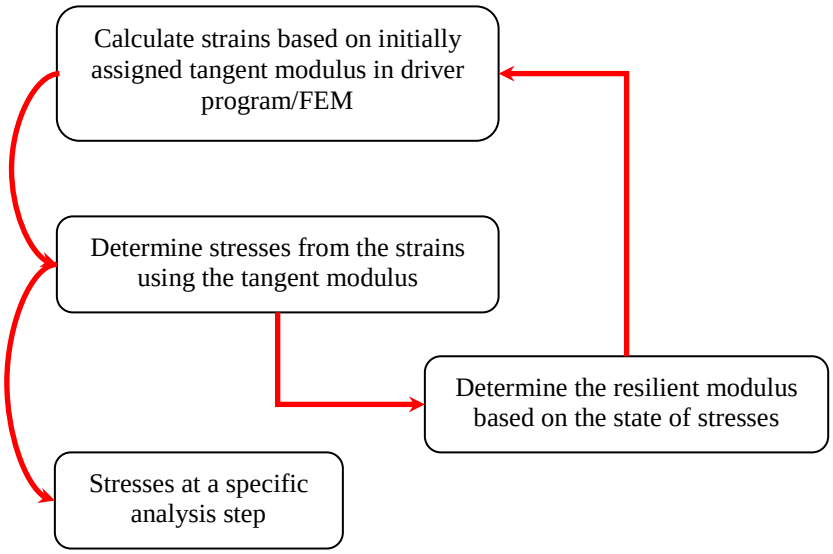

Figure 26: Incorporation of stress-dependency in a pavement model

After development of the FORTRAN subroutine, it needs to be evaluated. To date, a stress of 10 psi, ramping over time, is applied on a single element. Figure 27 shows that both bulk and octahedral shear stress vary linearly with vertical stress on a single element where the stress-hardening of base layer is incorporated through the subroutine. The reason behind this linear variation is because, the bulk stress is summation of three orthogonal stress components, i.e., $\theta = \sigma_1 + \sigma_2 + \sigma_3$, and the octahedral shear stress is: $\tau_{oct} = \sqrt{2}/3(\sigma_2 - \sigma_1)$ since $\sigma_1 \approx \sigma_3$.

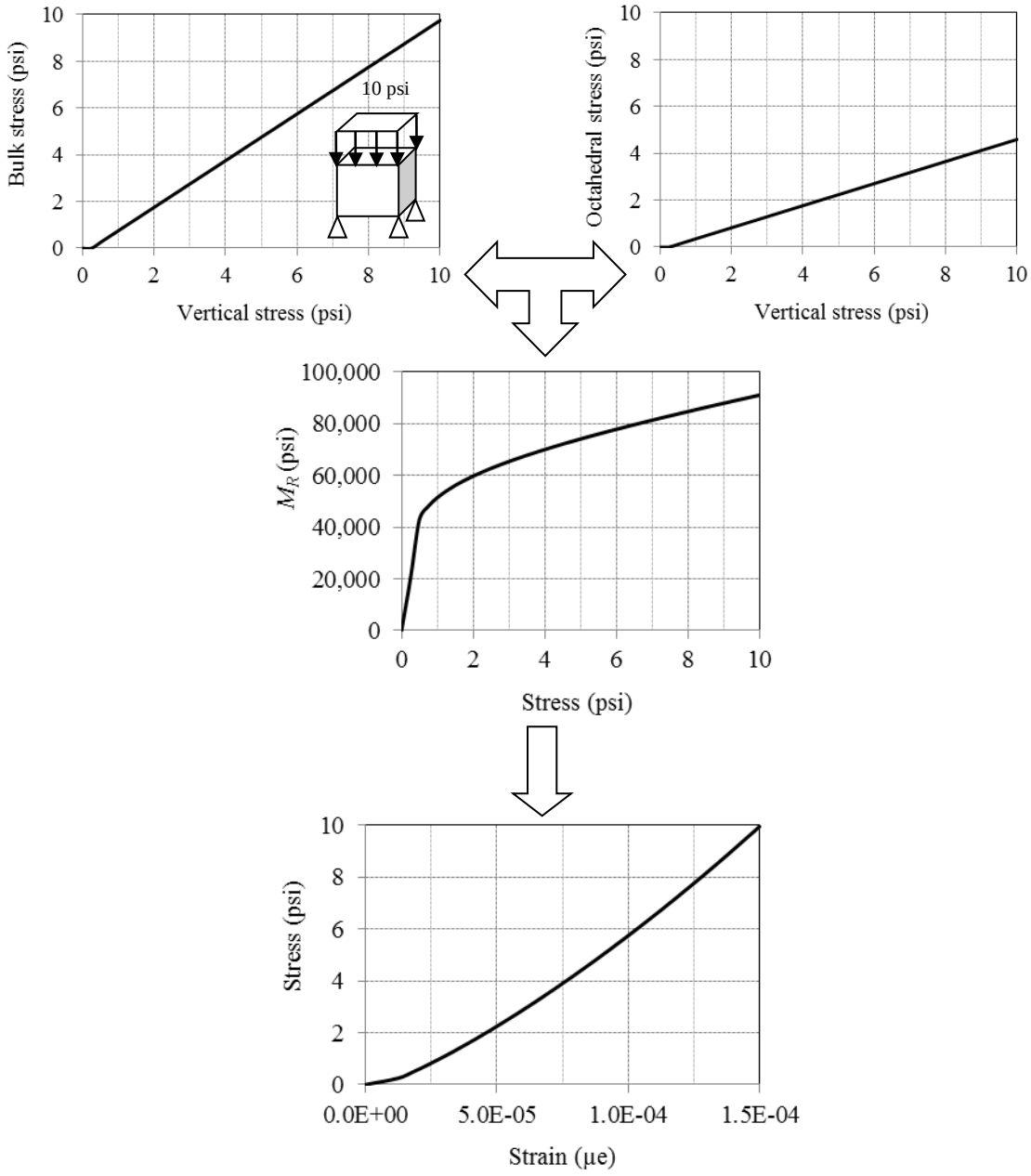

Figure 27: Stress-dependency in a single element analysis

Resilient modulus (M_r) is a nonlinear function of both bulk and octahedral shear stress. In addition, there is no negative regression coefficient in case of base layer. It leads to gradual increase in M_r with vertical stress which is the example of stress-hardening. At the end, it is observed that the nonlinear modulus results in nonlinear variation in vertical strain even after the application of linear varying vertical stress. At 10 psi, the resilient modulus is 90,000 psi and vertical strain is 150 microstrain.

In summary, the above mentioned observations indicate that the developed subroutine successfully integrates the stress-dependency and nonlinear elasticity to the dynamic FEM of pavement.

Combining Multiple Subroutines

The subroutines are now combined into a single FORTRAN code, i.e., driver subroutine. Figure 28 shows the outline of the subroutines. Subgrade is not included in this outline since it is assigned using the ABAQUS material library. Material parameters of the OGFC layer was collected from Tarefder and Islam (2015). This driver subroutine mainly contains two generalized models. These are: (a) cross-anisotropic, viscoelastic, and temperature-dependent; and (b) Stress-dependent and nonlinear elastic material models. The first one addresses both OGFC and AC layer where the OGFC is assumed as isotropic layer. The second one addresses both of the base and subbase layers. Goal of these material models is to provide the stiffness at the end of every analysis time step. This stiffness is used by the FEM program, i.e., dynamic analysis algorithm in ABAQUS, to determine stress-strain at time steps.

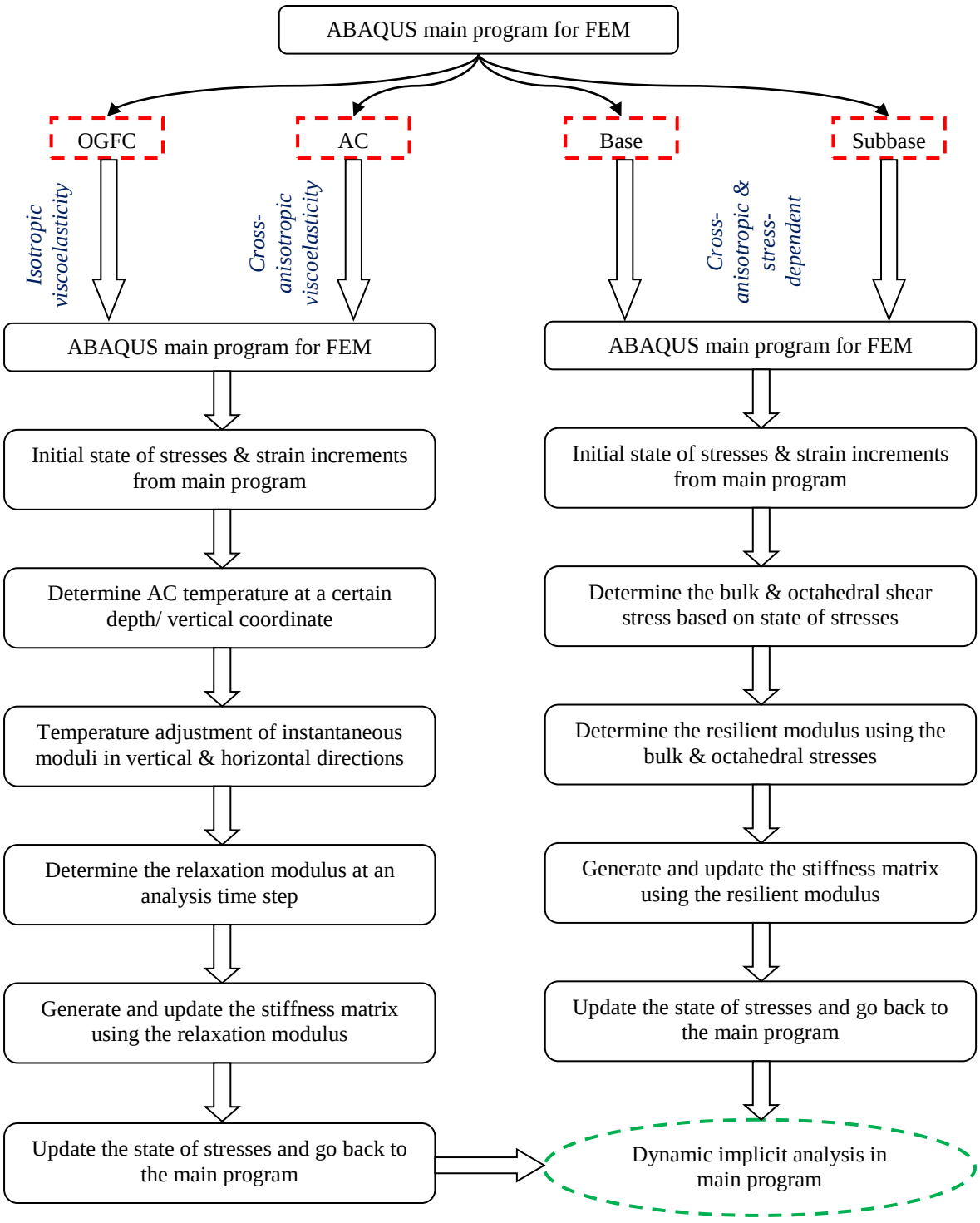

Figure 28: Outline of the combined subroutine

TASK 3: FIELD TESTING AND FEM MODEL VALIDATION

Strategy of the field testing and FEM model validation is illustrated in a flow chart (see Figure 29). FWD tests were conducted on the selected locations on the instrumented pavement sections. The selected locations were the locations where strain gauges and earth pressure cells were installed at the bottom of the AC layer and top of the unbound layers respectively. Pavement surface deflections, tensile strain from horizontal ASG, and vertical compressive stress from EPC were collected under the FWD test load, i.e., 9 kip.

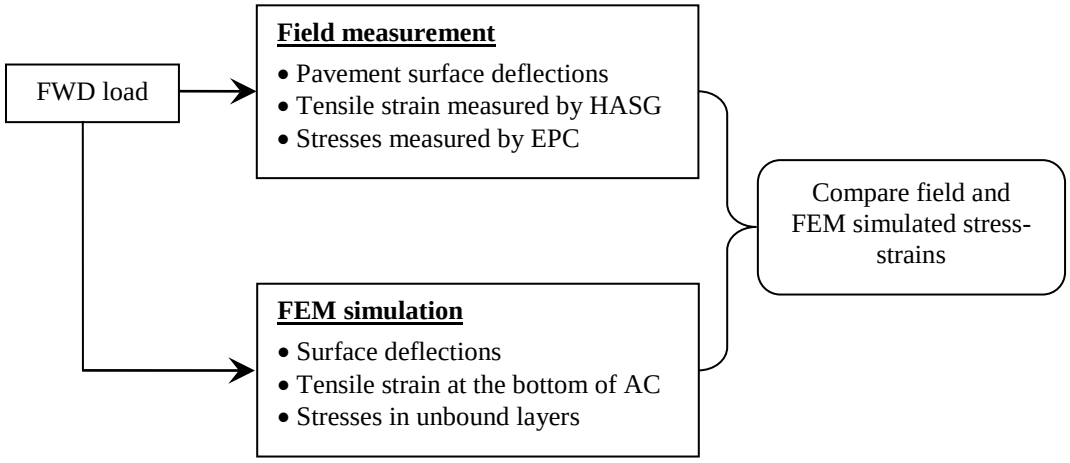

Figure 29: Validation of pavement FEM model

The dynamic FEM was simulated to determine the similar pavement responses under FWD test type load. Finally, simulate and field responses were compared for validation purpose.

Field vs. FEM

Stress and strains over time were also determined from the FEM simulation under the 9 kip load (with a duration 30 milliseconds). Figure 30(a) and (b) show the comparison between the simulated and measured pavement surface deflection. In Figure 30(a), the time-deflection history at center of the loading area from the FEM simulation is fairly close to that from the field measurement, i.e., FWD test. The peak deflections from at five different radial distances from FEM simulation and field measurement are compared in Figure 30(b). The field measured deflections are also close to that from the FEM simulation. The Root Mean Square of Error (RMSE, %) of the deflections is 7.9%.

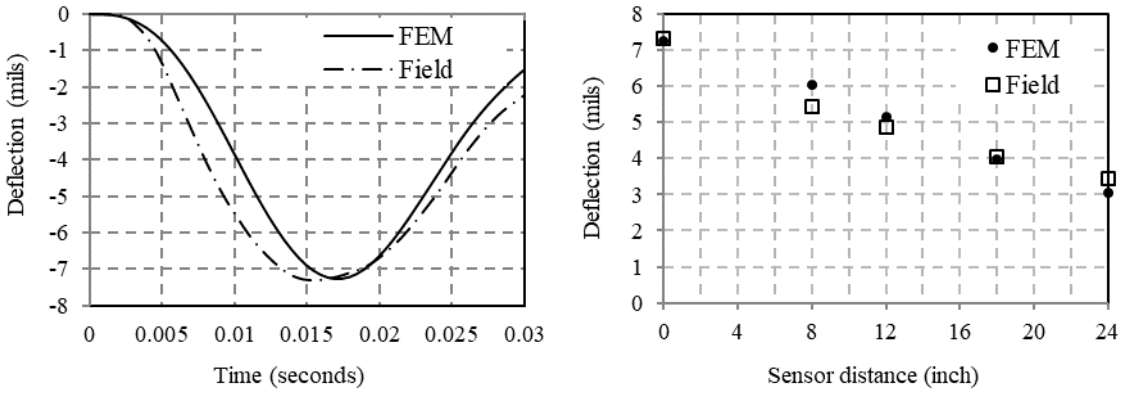

(a) Time-deflection history (b) Peak deflection

Figure 30: Comparison of pavement surface deflections (FEM vs. Field)

Table 3 summarizes both of the field measured and FEM predicted stresses and strain. The minimum (%) difference is 2.1, which is in case of horizontal tensile strain at the bottom of the AC layer. The vertical stresses were measured in middle of the base, top of the subbase, and 4 in. below from the subbase-subgrade interface in the subgrade. The stresses simulated by the FEM are fairly close to the field measured stresses with maximum (%) difference of 13.4.

Table 3: Comparison of pavement responses (Field vs. FEM)

Response	Field	FEM	(%) Difference
Tensile strain in AC (με)	75.4	73.8	2.1
Vertical stress in base (psi)	14.10	12.6	10.6
Vertical stress in subbase (psi)	10.85	9.4	13.4
Vertical stress in subgrade (psi)	5.28	4.84	8.3

Based on the comparison of time-deflection histories, peak deflections, and stress-strain at depths, it is observed that the FEM simulated pavement response is close to the field responses. Therefore, this FEM model can be used for further simulations in next steps of this study.

Distribution of Strains

The validated FEM is simulated under a non-uniform tire pressure. Vertical strains over the entire pavement domain and horizontal strains in asphalt layers are determined from the FEM simulation at two pavement surface temperatures, i.e., 9.9 and 35.4 ºC.

Vertical Strain — Contours of vertical strains at 9.9 and 35.1 ºC are plotted in Figure 31(a) and (b). Vertical strains are compressive in nature due to compressive tire-pavement contact stress and have negative sign in the contours. Strain variation over depth is not similar to the previous trends as observed in stress and deflection. Vertical strain in the AC layer is small even after the presence of high stress. This is due to greater magnitude of AC modulus. Underneath the AC layer, vertical strains are high in the unbound layers. The reason is that the unbound layer is very small compared to the AC modulus and thereby, vertical strain is high due vertical stress even below 20 psi. In every unbound layer, vertical strain is high at the top of a specific layer gradually diminishes with depth. It is also observed that there is a sudden strain variation at the

layer interfaces which is due to change in material stiffness/modulus. Finally, at low AC temperature (9.9 ºC), vertical strains are also small which is not only due to the temperature variation. At this temperature, unbound layers have the minimum moisture content which leads to higher base and subbase moduli.

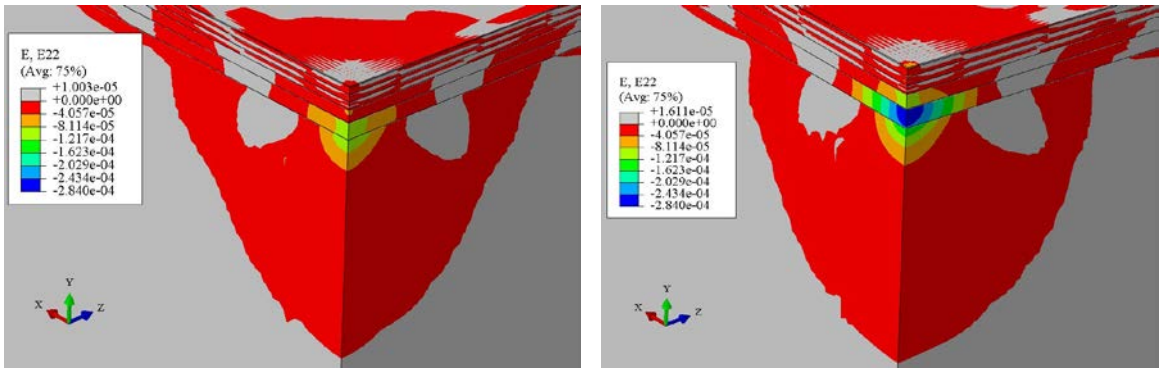

(a) Temperature: 9.9 ºC (b) Temperature: 35.1 ºC

Figure 31: Distribution of vertical strain

Horizontal Strain — Contours of horizontal strain in AC along traffic direction are plotted at 9.9 and 35.1 ºC respectively in Figure 32(a) and (b). Signs of tensile strains are positive in these figures. Similar to the distribution of longitudinal stress, longitudinal strains are also discontinuous at the AC-AC layer interfaces due to assignment of partial bonding condition at these interfaces. Tensile strain is developed at the bottom whereas the compressive strain is developed at the top of each of these AC layers/lifts. The entire OGFC layer shows compressive strain due to compressive longitudinal stress. Comparing the two contours, longitudinal tensile strain at high temperature is greater than that at low temperature.

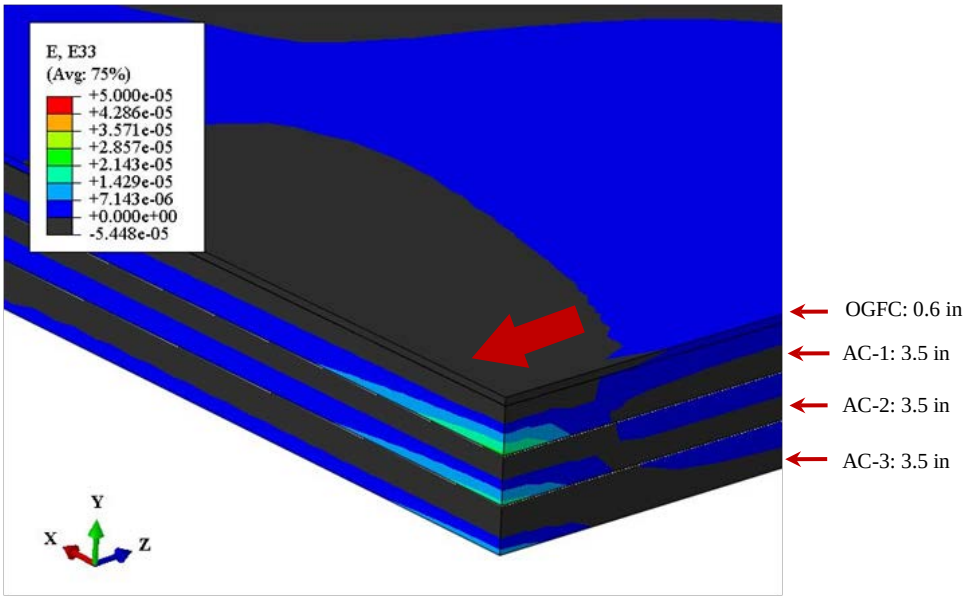

(a) Temperature: 9.9 ºC

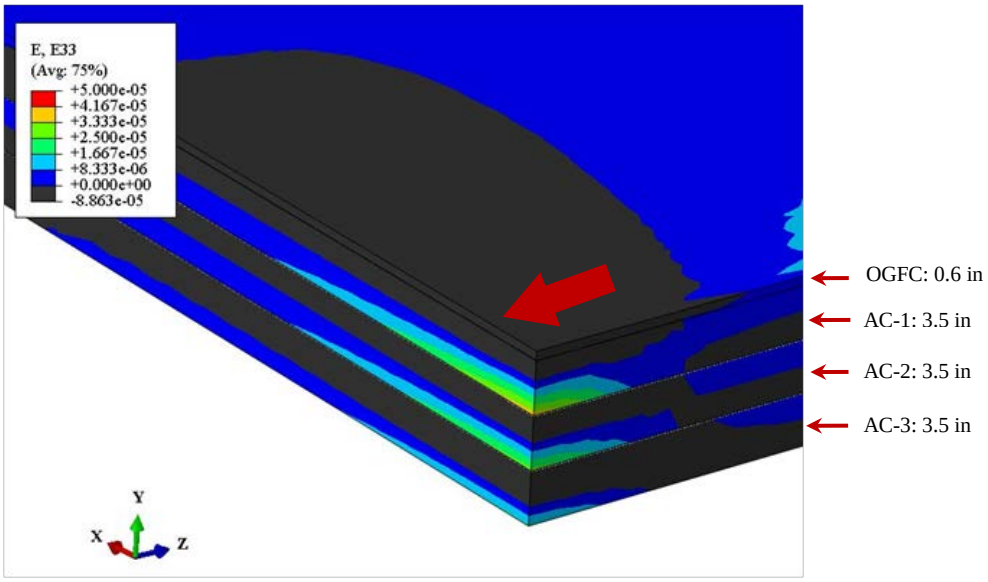

(b) Temperature: 35.1 ºC

Figure 32: Horizontal strain in AC sublayers

Only horizontal tensile strain at the bottom of the AC layer was compared since the vertical strain data was not available earlier. In this quarter, vertical strain in AC layer is also collected from the Vertical Asphalt Strain Gauge (VASG) in January 2017. The field vertical strain is 22.8 microstrain whereas the simulated strain is 26.6 microstrain.

TASK 4: DETERMINE THE EFFECTS OF ANISOTROPY ON RESPONSES

Goal of this task is to investigate the effect cross-anisotropy on pavement stress-strain. The full-scale FEM of instrumented pavement section is simulated at:

- Varying Degree of Cross-Anisotropy (*n*-value) in AC layer, i.e., $n = E_h / E_v$ where E_h = horizontal modulus and E_v = vertical modulus. During the FEM simulations, the *n* -value is varied from 0.25 to 1.0 (isotropy).
- Varying depth-temperature profiles in AC and moisture contents in unbound layers at different months over a year.

Adjustment of FEM Inputs

Depth-temperature profiles in four different months, namely, January, April, July, and September, are integrated to the AC layer during the simulations (see Figure 1). These profiles are assigned based on temperatures measured at varying depths, i.e., 0, 2, and 12 inches from the pavement surface. Temperature is constant over top 0.6 inch in the OGFC layer and gradually attenuates with depth. It is observed that temperature is the maximum in July and minimum in January respectively. These temperature trends and related modulus variation are assigned according to eqn. (20 - 21).

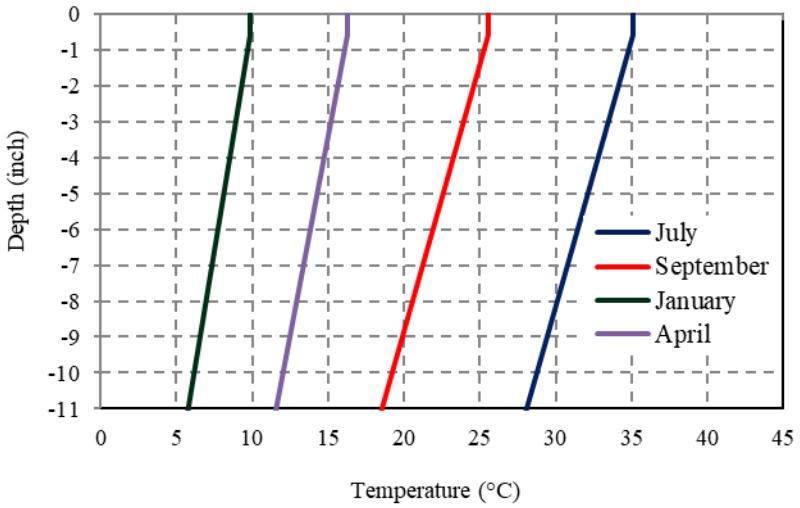

Figure 33: Flow chart of stress-dependency determination in different months

It was observed that the moisture level in unbound layers vary over a year (Tarefder and Islam 2015). Unbound layer modulus will also change due to this moisture variation, specially, during the earlier mentioned four months. There is need to introduce a set of adjustment factors to assign stress-dependency through eqn. (25).

Unbound layer moduli are adjusted for moisture contents in January, April, July, and September. FWD tests were conducted in the selected months to determine the base and subbase moduli through backcalculation process. Ratios of the backcalulated moduli ($R = E_i / E_{July}$, where i = January, April, July, and September) in those months are determined. These ratios are shown in Figure 34. The ratios for both base and subbase in July are 1.0 since the moduli in this month are

considered as reference. These ratios are the maximum in January since the moduli are the maximum in this month.

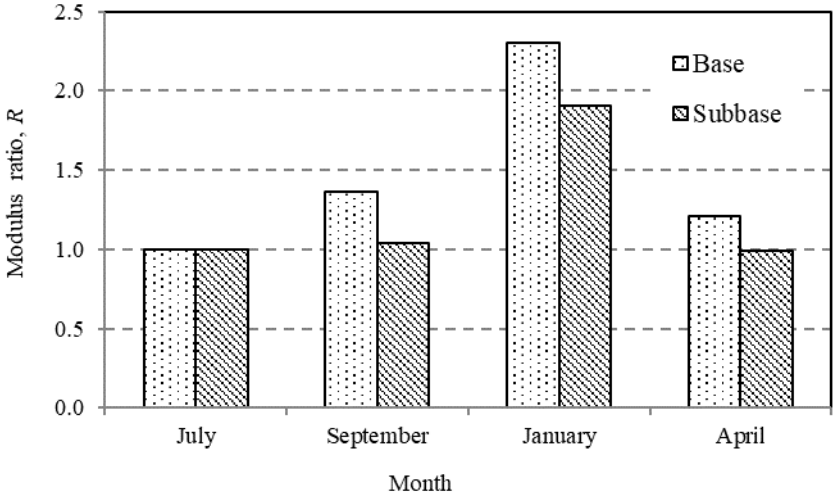

Figure 34: Base and subbase modular ratios in different months

The *R*-values are then multiplied with the k_1 - coefficient correspond to the month of July. Regression coefficients, i.e., k_1, k_2, and k_3, are summarized in Table 4. Here, only the k_1 - coefficient varies whereas the other two factors, namely, k_2 and k_3 - coefficients are same. The reason is that the nature of stress-dependency is assumed to be the same even though the modulus values will vary.

Table 4: Adjusted regression coefficients

Layer	Base			Subbase		
	k_1	k_2	k_3	k_1	k_2	k_3
January	12384	0.15	0.75	3285	0.17	-0.27
April	6490			1705		
July	5385			1722		
September	7358			1792		

Effect of AC Cross-Anisotropy on Stress-Strain

Tensile Strain in the AC Layer — The FEM is simulated to determine pavement stress-strain. Horizontal tensile strains at bottom of the AC layer are determined at varying *n*-values ($= E_h / E_v$) (see Figure 35(a)). It is observed that the tensile strain decreases as *n*-value increases towards isotropy, i.e., *n* =1.0. Based on the constitutive relationship for cross-anisotropic body, horizontal strain, $\varepsilon_h = \sigma_h / E_h - \nu_{vh}\sigma_v / E_v - \nu_{hh}\sigma_h / E_h$ where $E_v =$ vertical modulus, $E_h =$ horizontal modulus, $\sigma_v =$ vertical stress, $\sigma_h =$ horizontal stress, and $\nu_{vh}, \nu_{hh} =$ Poisson's ratio along vertical and horizontal planes respectively. The horizontal modulus increases with increase in *n*-value towards isotropy. Vertical stress distribution in AC layer shows that difference in stress due to cross-anisotropy variation is small (see Figure 35(b)). This difference is insignificant whenever

stress difference is compared to modulus difference. Therefore, it leads to a decrease in horizontal strain whenever horizontal modulus is increased towards the isotropy.

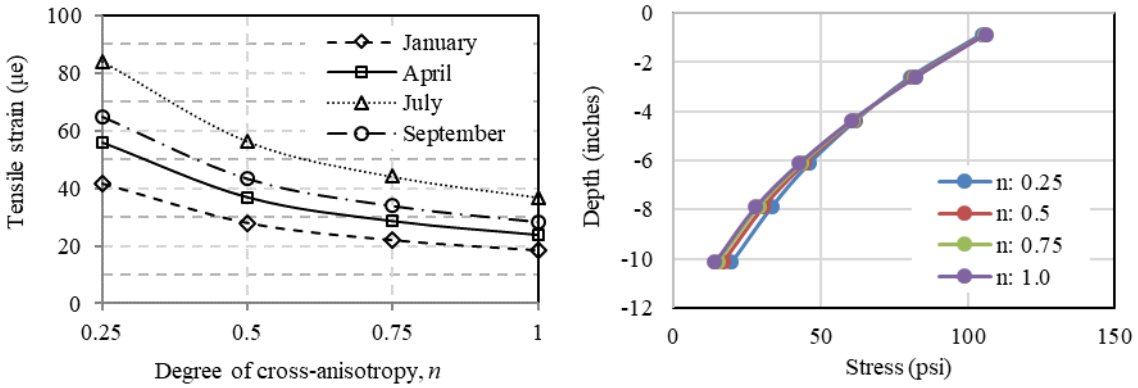

(a) Tensile strain (b) Vertical stress profile

Figure 35: Horizontal tensile strain at the bottom of AC layer

In addition, tensile strain in July is greater than that in any other month due to high temperature in the AC layer. In July, difference in strain between *n*-value of 0.25 and 1.0 is more than 40 microstrain whereas that is about 20 microstrain in January. In summary, tensile strain at the bottom of the AC layer is sensitive to both cross-anisotropy and temperature variation in AC layer.

Vertical Strains in the Pavement Layers — Vertical strains are determined at mid-depth of AC, base, subbase, and top of the subgrade at varying *n*-values. Figure 36(a) through (d) shows the variation of vertical strains in pavement layers at varying *n*-values in different months. The common observation is that the vertical strains are the maximum in July whereas those are the minimum in January due to the temperature variation. In addition, the strains decrease with increase in n-value towards 1.0 (isotropy). Differences in strains in AC, base, subbase, and subgrade are about 15.1, 44.3, 69.9, and 39.5 microstrain, respectively, in July and these are the maximum compared to those in other months. The minimum strain differences are observed in January and these are about 7.5, 18.7, 28.0, and 32.8 microstrain in AC, base, subbase, and subgrade respectively. Based on the constitutive relationship for cross-anisotropic body, horizontal strain, $\varepsilon_v = \sigma_v / E_v - 2\nu_{vh}\sigma_h / E_v$ where $E_v =$ vertical modulus, $\sigma_v =$ vertical stress, $\sigma_h =$ horizontal stress, and $\nu_{vh} =$ Poisson's ratio along vertical plane. Change in horizontal modulus does not affect the vertical strain directly. Instead, vertical stress distribution variation is the main factor in this case. It is mentioned earlier that stress in AC layer varies with cross-anisotropy even though it is small. It leads to a vertical strain variation in AC layer which is small compared to the unbound layers.

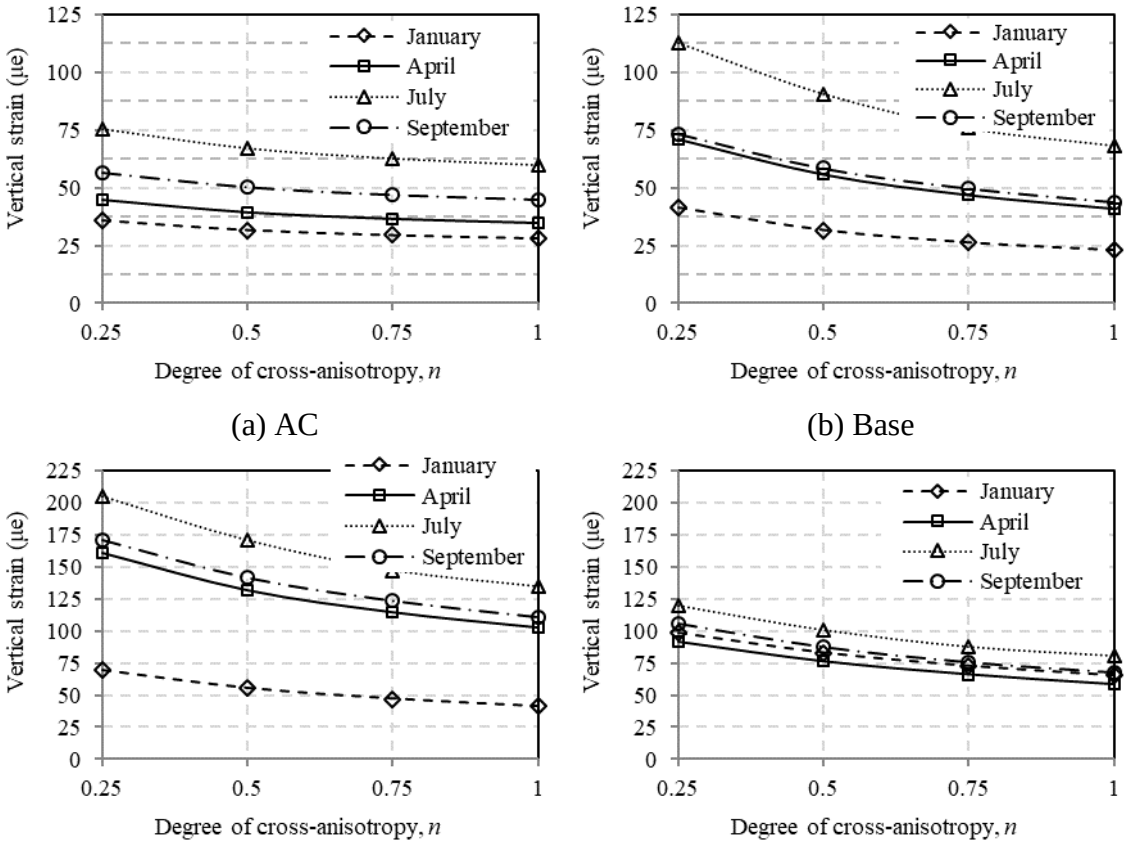

Figure 36: Vertical strain in pavement layers

It is observed that difference in the vertical strain due to cross-anisotropy variation is very high in both base and subbase. The reason may be due to the variation in stress-dependent modulus of unbound layers. Figure 37(a) and (b) show the variation of vertical stress with *n*-value of the AC in four different months. Stress decreases as the *n*-value increases in those months. In addition, stresses in both base and subbase are the maximum at high temperature in July due to the least stiffness of the AC. It indicates that the base and subbase moduli are expected to decrease with increase in *n*-value since the stress also decreases in those layers. The reason is that a decrease in vertical stress will lead to a decrease in both bulk and octahedral shear stresses. Finally, the unbound layer modulus will also decrease since it depends on the earlier mentioned stresses.

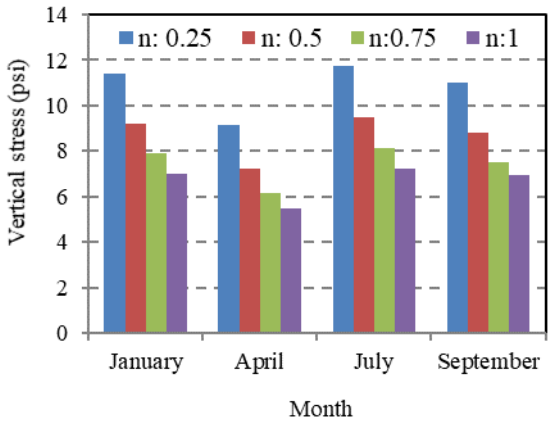

(a) Vertical stress in base

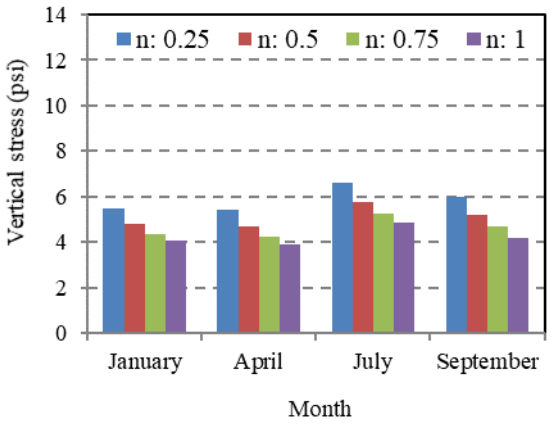

(b) Vertical stress in subbase

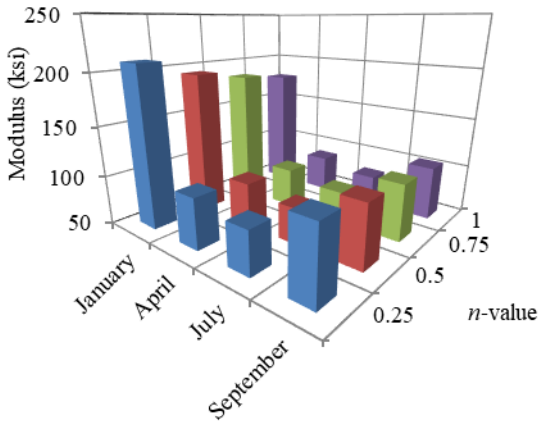

(c) Modulus in base

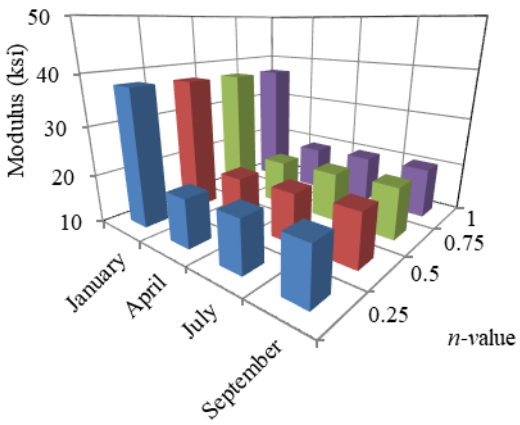

(d) Modulus in subbase

Figure 37: Vertical nonlinear modulus in unbound layers

Later, the expected trend is observed in Figure 37(c) and (d). Base modulus is greater than subbase modulus and the rate of modulus decrease is also high in base layer. Moduli in both of the layers are the maximum in January and minimum in July respectively. The main reason for this monthly variation of the modulus is the varying regression coefficient, k_1, which is the maximum in January. It is observed earlier that the vertical strain decreases with increase in *n*-value. The reason is that the rate of stress decrease is higher than the rate of decrease in modulus.

Vertical strain variation in subgrade is smaller compared to the other unbound layers. The reason is that stress attenuates with depth and approaches to 3.9-5.3 psi in subgrade at varying cross-anisotropy. In addition, this layer is assumed as linear elastic. Therefore, modulus does not change due to stress variation. It is known that subgrade modulus is smaller than the base and subbase modulus. It indicates that the ratio of stress and modulus leads to strain variation due to cross-anisotropy, however, this variation is smaller compared to the other unbound layers due to smaller values of stress in subgrade.

Overall, both horizontal tensile strain at the bottom of the AC layer and vertical strains in pavement layers are sensitive to variation of cross-anisotropy in AC layer. Tensile strain variation due to cross-anisotropy is enhanced whenever pavement temperature is high.

Base Isotropy vs. Cross-anisotropy

In this step, the FEM simulations are also performed in presence of cross-anisotropic base layer, i.e., n = 0.25. Goal is to investigate whether pavement response sensitivity due to AC cross-anisotropy is enhanced in presence of unbound layer cross-anisotropy or not. Trends of pavement strains due to these controlled variation of cross-anisotropy is discussed as follows:

Tensile Strain in the AC Layer — Figure 38 shows the variation of the tensile strain with *n*-value of the AC in presence of both base isotropy and cross-anisotropy. It is observed that the tensile strain decreases as *n*-value increases towards isotropy, i.e., n =1.0. The reason is that the horizontal stiffness is smaller than vertical stiffness whenever *n*-value is smaller than 1.0 (isotropy). The strain values increase whenever the base cross-anisotropy is incorporated, i.e., *n*-value of the base is 0.25. It was mentioned during the FEM development that the friction coefficient along the base-AC interface is assumed as 1.0. Compressive horizontal stress on the top of the base layer along this interface drops whenever base layer is considered cross-anisotropic. It leads to an increase in tensile strain at the bottom of the AC layer.

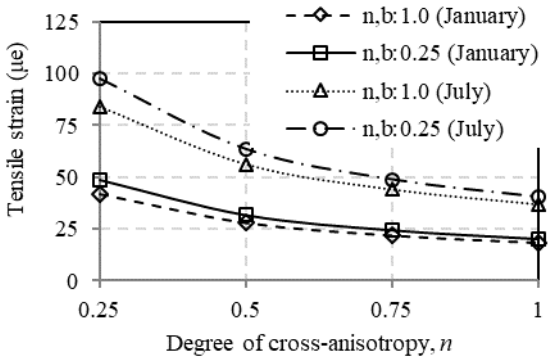

Figure 38: Horizontal tensile strain in AC (isotropic vs. cross-anisotropic base)

In summary, reduction in horizontal stiffness of the base layer also causes an increase in tensile strains at the bottom of the AC layer.

Vertical Strains in the Pavement Layers — Figure 39(a) through (d) show the variation of vertical strains in pavement layers at varying *n*-values in presence of base isotropy and cross-anisotropy. In both cases, vertical strains are the maximum in July whereas those are the minimum in January. The reason is that both AC and unbound layer moduli are the minimum in July which is opposite to January. In addition, the strains decrease with increase in *n*-value towards 1.0 (isotropy) as before. Values of the vertical strains are enhanced whenever the *n*-value of the base layer is 0.25. In addition, amount of this strain increase is pronounced at high temperature. Strains in the pavement layers are highly sensitive to temperature, except, subgrade.

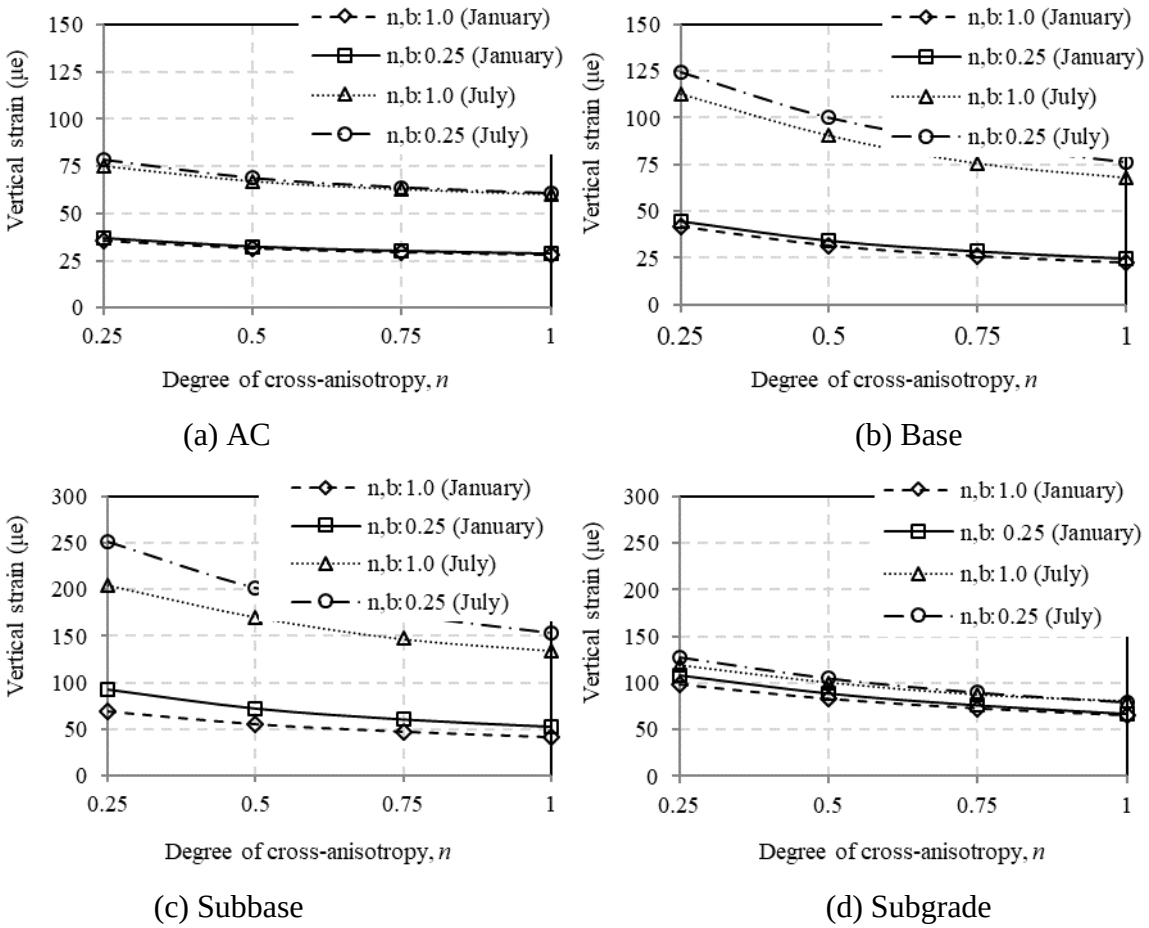

Figure 39: Vertical strain in pavement layers (isotropic vs. cross-anisotropic base)

It is observed that difference in the vertical strain due to cross-anisotropy variation is very high in both base and subbase due to the variation in stress-dependent modulus of unbound layers. Figure 40(a) and (b) show the variation of vertical stress with *n*-value of the AC in January and July considering both base isotropy and cross-anisotropy. Stress decreases as the n-value of the AC increases in those months. In addition, stresses in both base and subbase are the maximum at high temperature in July due to the least stiffness of the AC. It indicates that the base and subbase moduli are expected to decrease with increase in *n*-value since the stress also decreases in those layers. The expected trend is evident in Figure 40(c) and (d). Moduli in both of the layers are the maximum in January and minimum in July respectively due to the similar trend of variation in regression coefficient, k_1, which is the maximum in January.

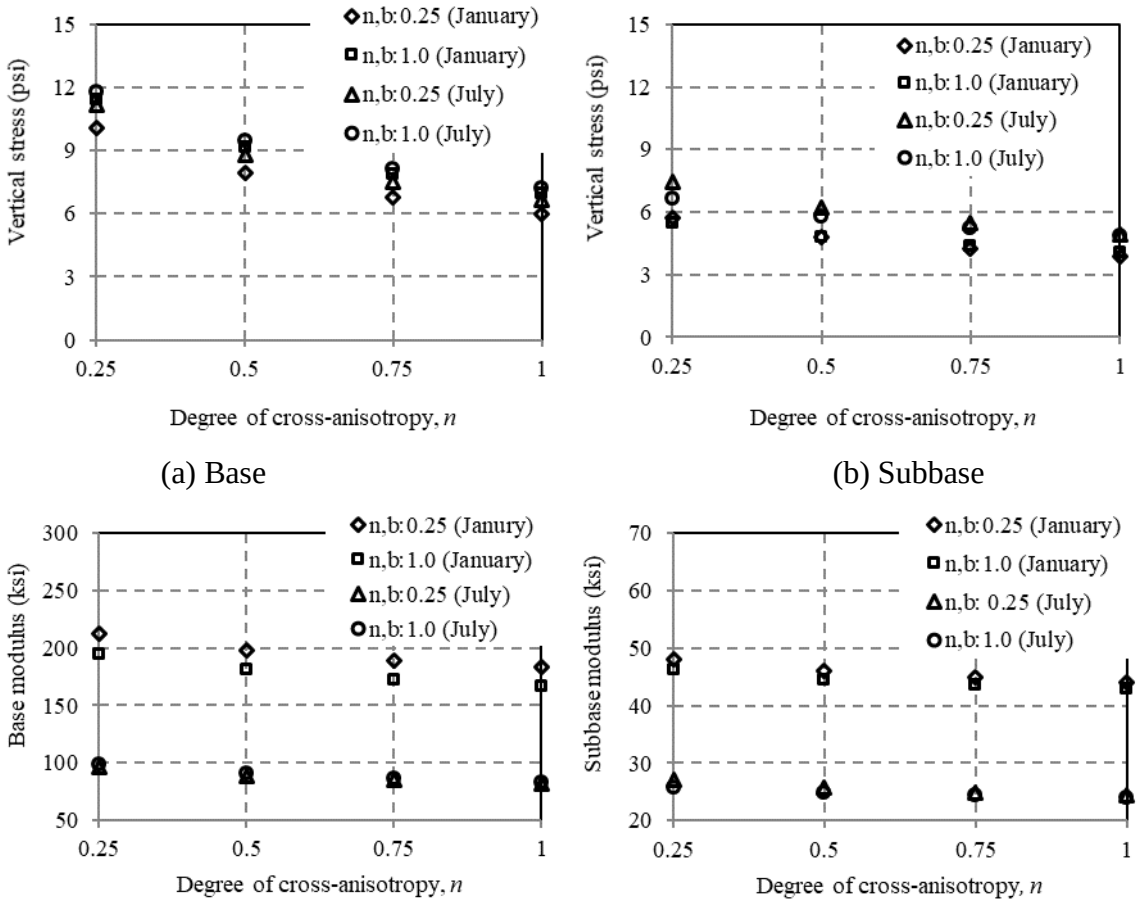

(a) Base (b) Subbase

(c) Base (d) Subbase

Figure 40: Vertical stress and modulus in unbound layers

Variations in stress and modulus due to incorporation of base cross-anisotropy are relatively small. However, the resulted vertical strains are high. This happens due to the decrease in stiffness/moduli (E_1 and E_3) in the horizontal plane which leads to smaller values of stresses (σ_1 and σ_3) in same plane. In summary, vertical strains in AC, and unbound layers will be enhanced in presence of the unbound layer cross-anisotropy due to decrease in stresses in the horizontal plane.

Linear vs. Nonlinear Elastic Base Layer

The FEM simulations are also performed for both linear and nonlinear elastic base layer whenever *n*-value of AC is varied following the earlier trend. Trends of pavement strains are discussed as follows:

Tensile Strain in the AC Layer — Figure 41 shows the variation of the tensile strain for linear and nonlinear elastic unbound layers, i.e., base and subbase, at two different temperatures. The tensile strain decreases as *n*-value increases towards isotropy, i.e., n =1.0, which is similar to the earlier observations. Incorporation of unbound layer nonlinearity enhances the values of tensile strain. Finally, tensile strain is sensitive to the temperature as expected.

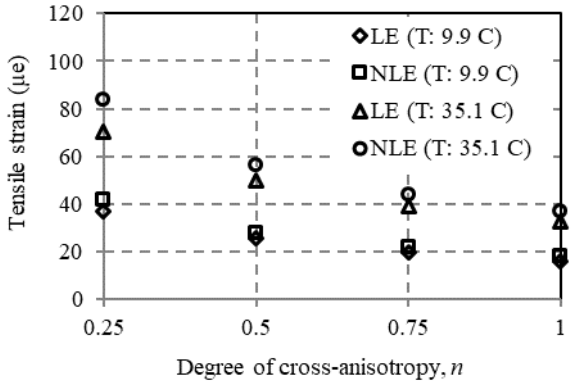

Figure 41: Tensile strain in AC layer (Linear vs. nonlinear elastic)

Vertical Strains in Pavement Layers — Figure 42(a) through (d) shows the variation of vertical strains in pavement layers at varying *n*-values for linear and nonlinear elastic unbound layers at two different temperatures. The vertical strains in the layers decreases with increase in *n*-value which are also sensitive to temperature variation which agrees with the earlier trends. It is also observed that the incorporation of nonlinear unbound layer leads to increase in vertical strains. However, in case of subgrade, vertical strain due to linear base and subbase layer is greater than that due to nonlinearity.

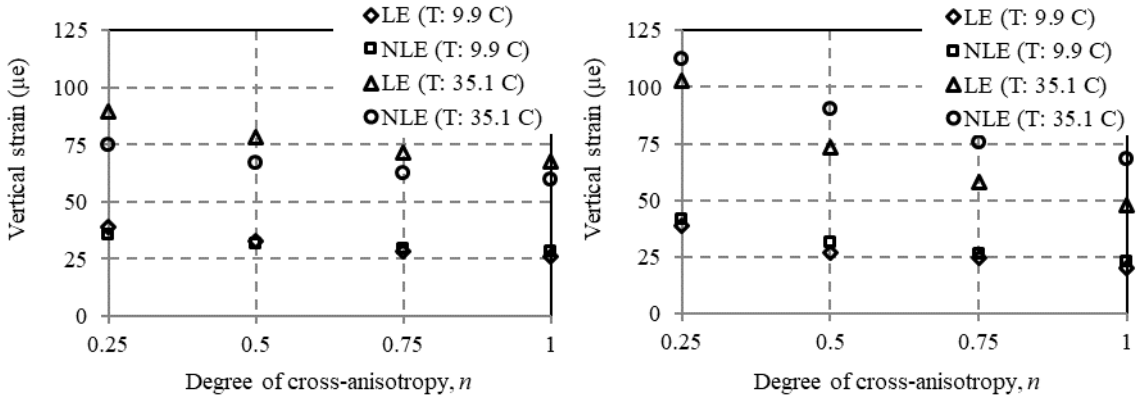

(a) AC (b) Base

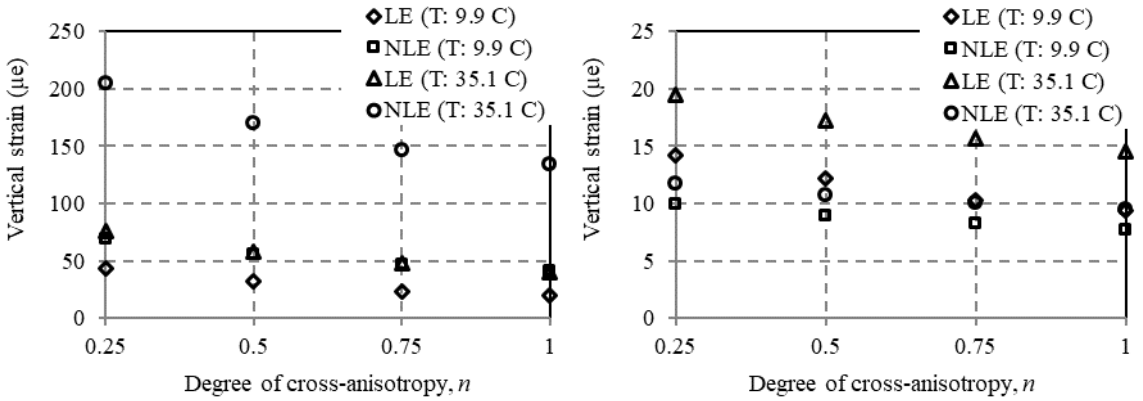

(c) Subbase (d) Subgrade

Note: LE – Linear Elastic and NLE – Non-Linear Elastic

Figure 42: Vertical strains in pavement layers (Linear vs. nonlinear elastic)

In summary, vertical strains in pavement layers decrease with increase in *n*-value of the AC towards the isotropy in both cases of linear and nonlinear elastic unbound layers. In addition, these strains are sensitive to temperature. In case of base and subbase, vertical strains based on nonlinear elasticity are greater than those based on linear elasticity.

TASK 5: DETERMINE THE EFFECTS OF ANISOTROPY ON PERFORMANCES

Goal of this task is to investigate the effect cross-anisotropy of AC layer on pavement performance such as damage. It is a typical practice that pavement performance is evaluated based on accumulated damage which is determined by the Miner's formula incorporating pavement strains (Rajbongshi 1997 and Huang 2004). According to this formula, the damage is calculated as follows:

$$D = \sum \frac{n}{N} \tag{30}$$

where $D =$ damage factor (0~1), $n =$ actual number of load repetition, and $N =$ number of load repetition till failure. This damage is suggested to calculate based on two major criteria: fatigue and permanent deformation. In case of fatigue and permanent deformation, eqn. (30) will be as follows:

$$D_f = \sum \frac{n}{N_f} \tag{31}$$

$$D_d = \sum \frac{n}{N_d} \tag{32}$$

where $D_f =$ damage factor due to fatigue, $D_d =$ damage factor due to permanent deformation, $N_f =$ number of load repetition till failure due to fatigue, and $N_d =$ number of load repetition till failure due to permanent deformation. The Asphalt Institute (Asphalt Institute 1982) proposed the following regression equations to calculate the N_f and N_d:

$$N_f = 0.0796\varepsilon_t^{-3.291} E_h^{-0.854} \tag{33}$$

$$N_d = 1.365\varepsilon_c^{-4.477} \tag{34}$$

where $\varepsilon_t =$ tensile strain at the bottom of the AC, $E_h =$ modulus of elasticity of AC along horizontal direction, and $\varepsilon_c =$ vertical compressive strain. In this study, $E_h = nE_v$, where $n =$ degree of cross-anisotropy. Incorporating the cross-anisotropy, Eqns. (33) and (34) can be modified as follows for a specific period and loading type:

$$D_{f,anis} = \frac{n}{0.0796n^{-0.854}\varepsilon_{t,anis}^{-3.291} E_v^{-0.854}} \tag{35}$$

$$D_{d,anis} = \frac{n}{1.365\varepsilon_{c,anis}^{-4.477}} \tag{36}$$

Eqns. (35) and (36) will be as follows whenever the material is assumed as isotropic:

$$D_{f,iso} = \frac{n}{0.0796\varepsilon_{t,iso}^{-3.291} E_v^{-0.854}} \tag{37}$$

$$D_{d,iso} = \frac{n}{1.365\varepsilon_{c,iso}^{-4.477}} \tag{38}$$

Now, damage due to single load repetition is defined by ratio of cross-anisotropic damage to isotropic damage for both fatigue and permanent deformation. Relationships of the damages per load repetition are as below:

Fatigue: $$\frac{D_{f,anis}}{D_{f,iso}} = n^{0.854}\left(\frac{\varepsilon_{t,anis}}{\varepsilon_{t,iso}}\right)^{3.291} \tag{39}$$

Permanent deformation: $$\frac{D_{d,anis}}{D_{d,iso}} = \left(\frac{\varepsilon_{c,anis}}{\varepsilon_{c,iso}}\right)^{4.477} \tag{40}$$

Eqns. (39) and (40) will be used throughout this study as a pavement performance evaluation indicator to investigate the effect of cross-anisotropy on pavement performance.

Base Isotropy vs. Cross-anisotropy

Tensile Strain in the AC Layer — The ratio of horizontal tensile strain considering cross-anisotropy and isotropy are calculated for incorporating both base isotropy and cross-anisotropy. The strain ratios at varying cross-anisotropy due to the maximum and minimum (July and January) temperatures are plotted in Figure 43(a). At both of these temperatures, strain ratios decrease as the *n*-value increases towards isotropy. It is also observed that strain ratios are enhanced due to incorporation of the base cross-anisotropy, i.e., *n,b*: 0.25.

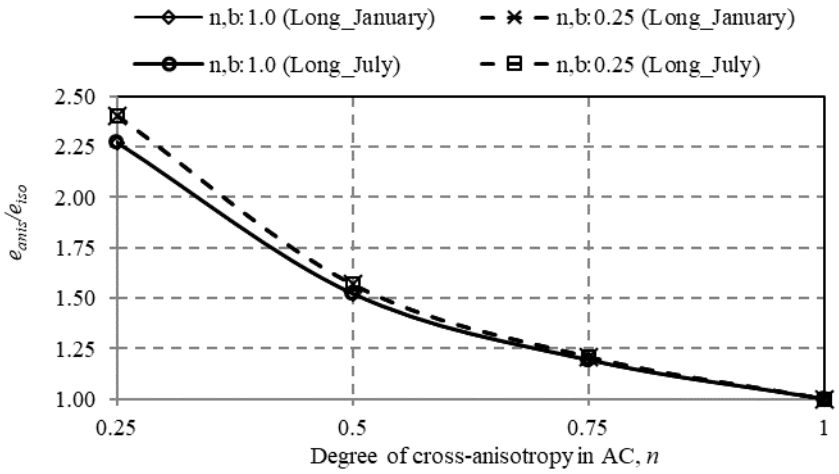

(a) Strain ratio

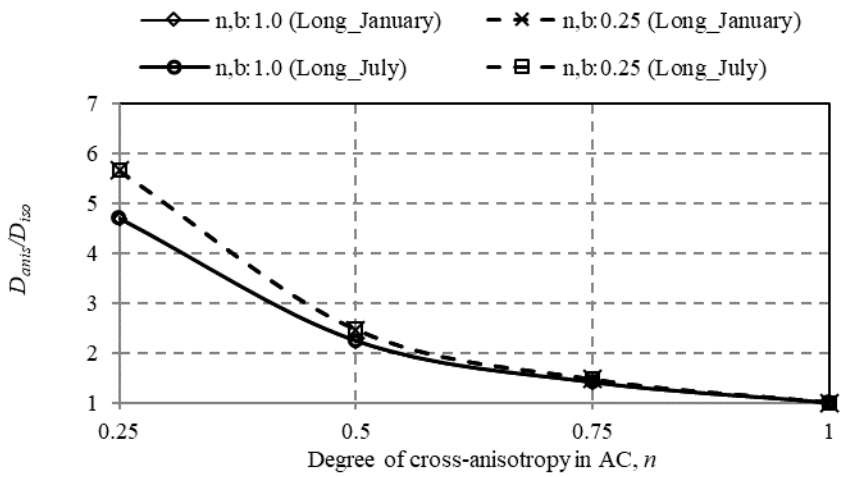

(b) Damage

Note: n,b – Degree of cross-anisotropy in base layer

Figure 43: Tensile strain ratio and damage in AC (isotropic vs. cross-anisotropic base)

Figure 43(b) shows the variation of damage for isotropic and cross-anisotropic base layer. The damage ratio follows the similar trend of the strain ratio where it decreases with increase in *n*-values. Presence of base cross-anisotropy enhances the values of the damage ratios.

In summary, tensile strains at the bottom of the AC layer increases due to incorporation of the base cross-anisotropy. Later, it results the enhanced damage per loading repetition. Unlike to earlier observations, the damage ratio incorporating base cross-anisotropy is sensitive to pavement temperatures.

Vertical Strains in the Pavement Layers — The vertical strain ratios in pavement layers at varying cross-anisotropy and temperatures are plotted in Figure 43. The minimum and maximum pavement temperatures in January and July respectively are selected for these plots. Strain ratios decrease as the *n*-value increases towards isotropy (see Figure 44(a) and (b)). The strain ratios in unbound layers are greater than that in the AC layer. It is also observed that the strain ratios are sensitive to the pavement temperatures. This ratio is high at low temperature and vice versa.

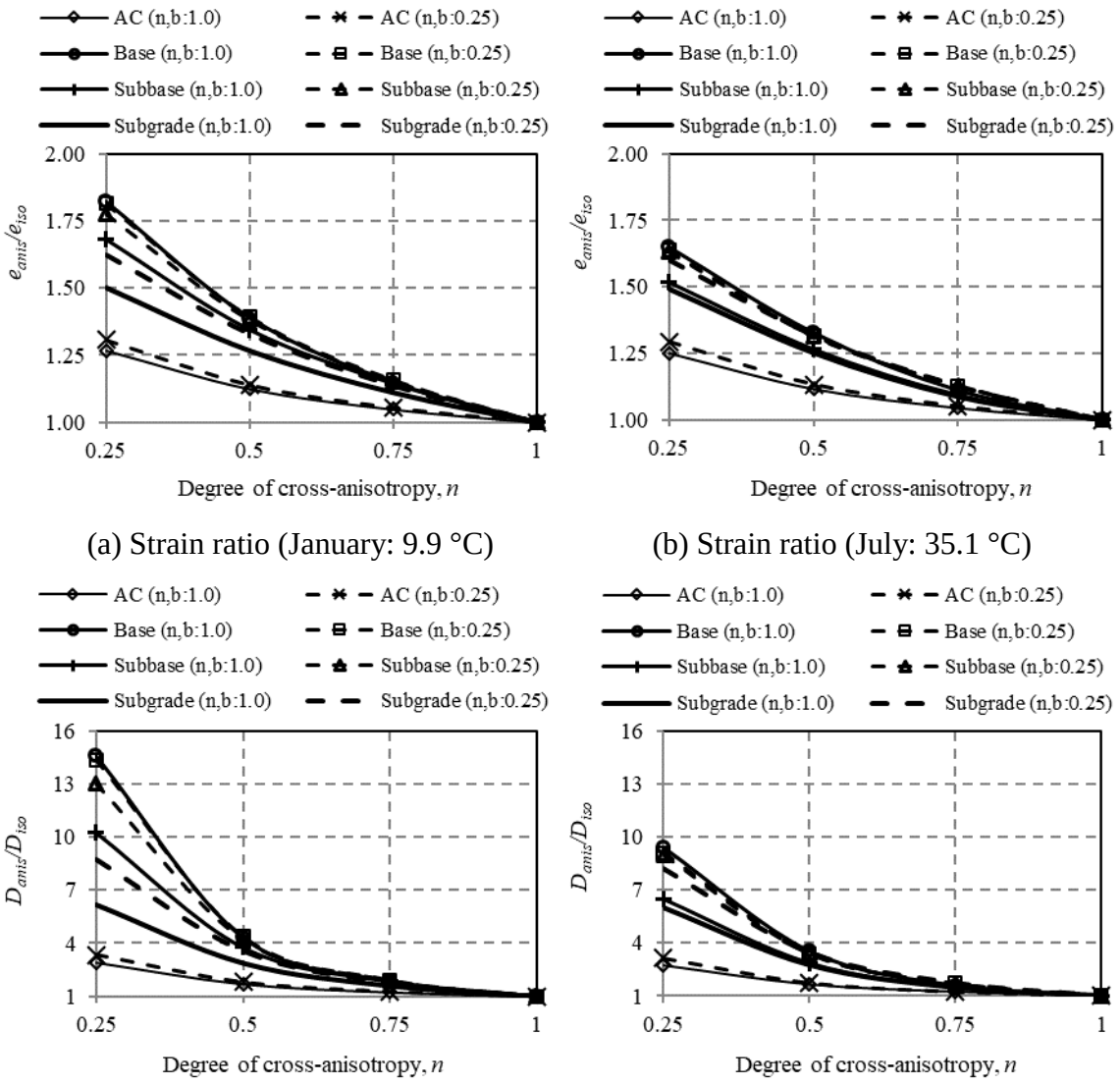

(a) Strain ratio (January: 9.9 °C)

(b) Strain ratio (July: 35.1 °C)

(c) Damage (January: 9.9 °C)

(d) Damage (July: 35.1 °C)

Note: n,b – Degree of cross-anisotropy in base layer

Figure 44: Vertical strain ratio and damage in pavement layers (isotropic vs. cross-anisotropic base)

Figure 44(c) and (d) show the variation of damage based on vertical strain ratios incorporating base cross-anisotropy. The damage ratio follows the similar trend of the vertical strain ratio where it decreases with increase in *n*-values. The damage ratios are sensitive to temperature variation. It is observed that this ratio is high at low temperature in January and vice versa. In summary, the relative damage per loading repetition is the high in January whenever the pavement temperature is low.

Linear vs. Nonlinear Elastic Base Layer

Tensile Strain in the AC Layer — The ratio of horizontal tensile strain ratios incorporating linear and nonlinear elastic base and subbase are calculated for both longitudinal and transverse. The

strain ratios at varying cross-anisotropy and temperatures are plotted in Figure 45(a) and (b). Strain ratios along both longitudinal and transverse directions decrease as the *n*-value increases towards isotropy. At high temperature, strain ratios considering nonlinear elasticity are greater than those considering linear elasticity. At and above *n*-value of 0.5, the ratios are same for both linear and nonlinear elasticity.

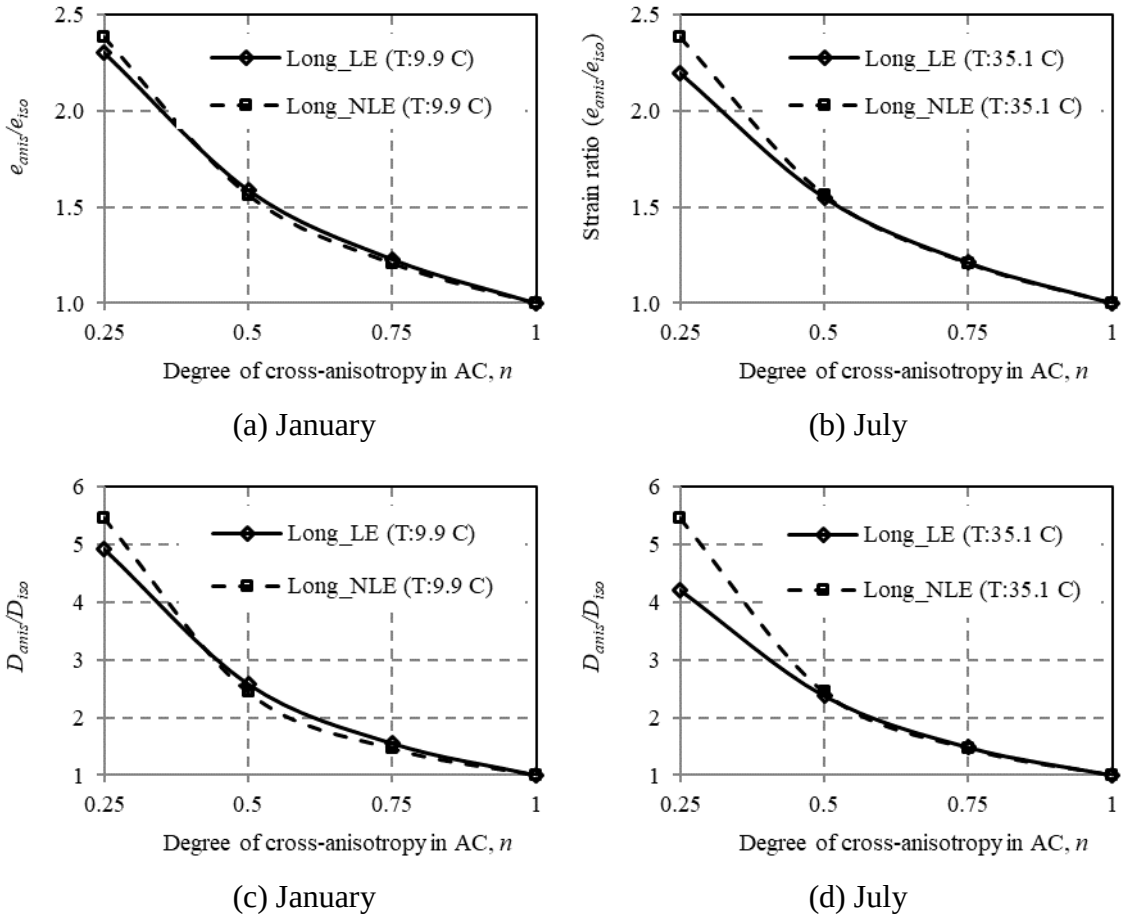

Note: LE – Linear Elastic and NLE – Non-Linear Elastic

Figure 45: Tensile strain ratio and damage

Figure 45(c) and (d) show the variation of damage for linear and nonlinear elastic base and subbase. The damage ratio follows the similar trend of the strain ratio where it decreases with increase in *n*-values. Damage ratio based on transverse strain is greater than that based on longitudinal strain at high temperature. Finally, presence of unbound layer nonlinear elasticity enhances the values of the damage ratios.

In summary, tensile strains at the bottom of the AC layer increases due to incorporation of the unbound layer nonlinearity at high temperature. Consequently, it results the enhanced damage per loading repetition.

Vertical Strains in the Pavement Layers — Vertical strain ratios in pavement layers at varying cross-anisotropy incorporating unbound layer nonlinearity are plotted in Figure 46(a) through

(d). Strain ratios decrease as the *n*-value increases towards isotropy as expected. The strain ratios in the base and subbase are greater than those in the AC and subgrade. Strain ratios are affected by temperature variations However, there is no regular trend. It is also observed that the strain ratios are high for linear elastic unbound layers.

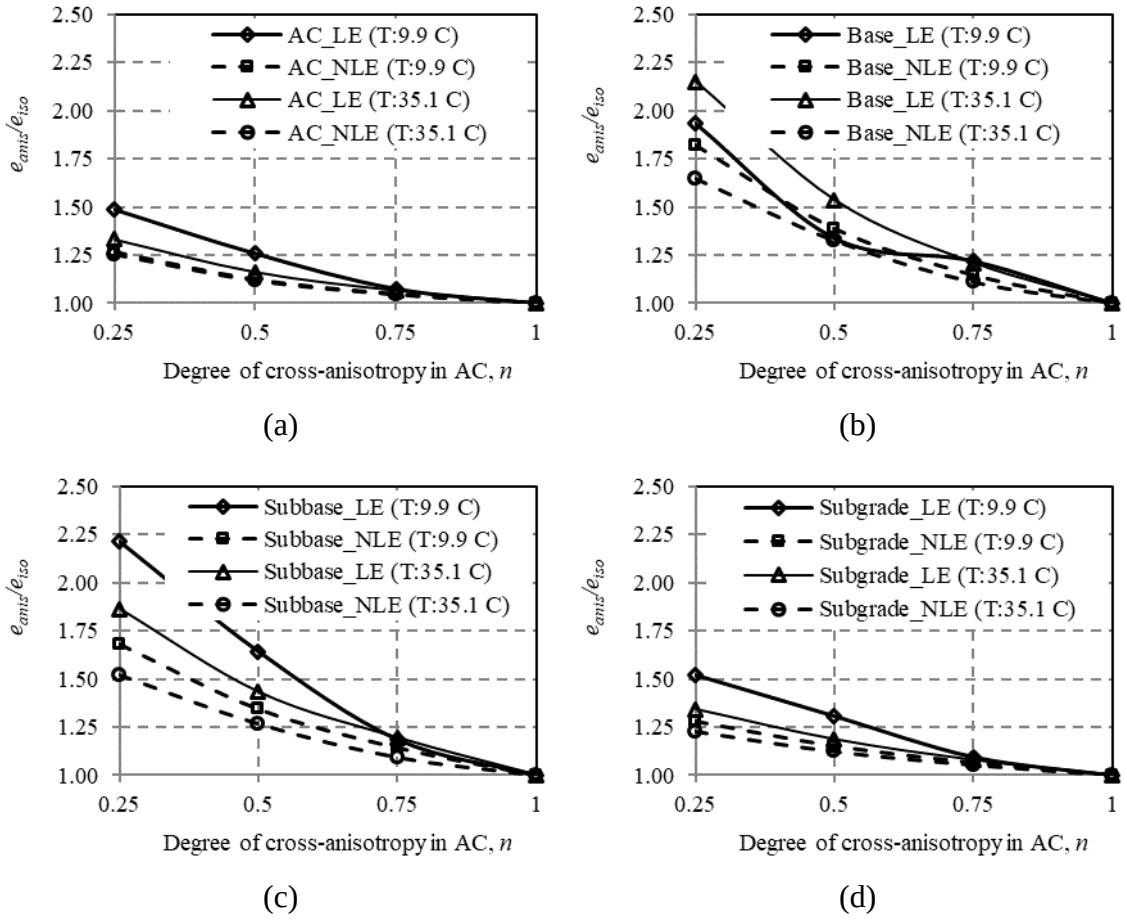

Note: LE – Linear Elastic and NLE – Non-Linear Elastic

Figure 46: Vertical strain ratios in: (a) AC, (b) Base, (c) Subbase, and (d) Subgrade

Figure 47(a) through (d) show the variation of damage based on vertical strain ratios incorporating unbound layer nonlinearity. The damage ratio follows the similar trend of the vertical strain ratio where it decreases with increase in *n*-values. The damage ratios in the base and subbase are greater than those in the AC and subgrade. In addition, these ratios based on linear elasticity are greater than that based on nonlinear elasticity in unbound layer.

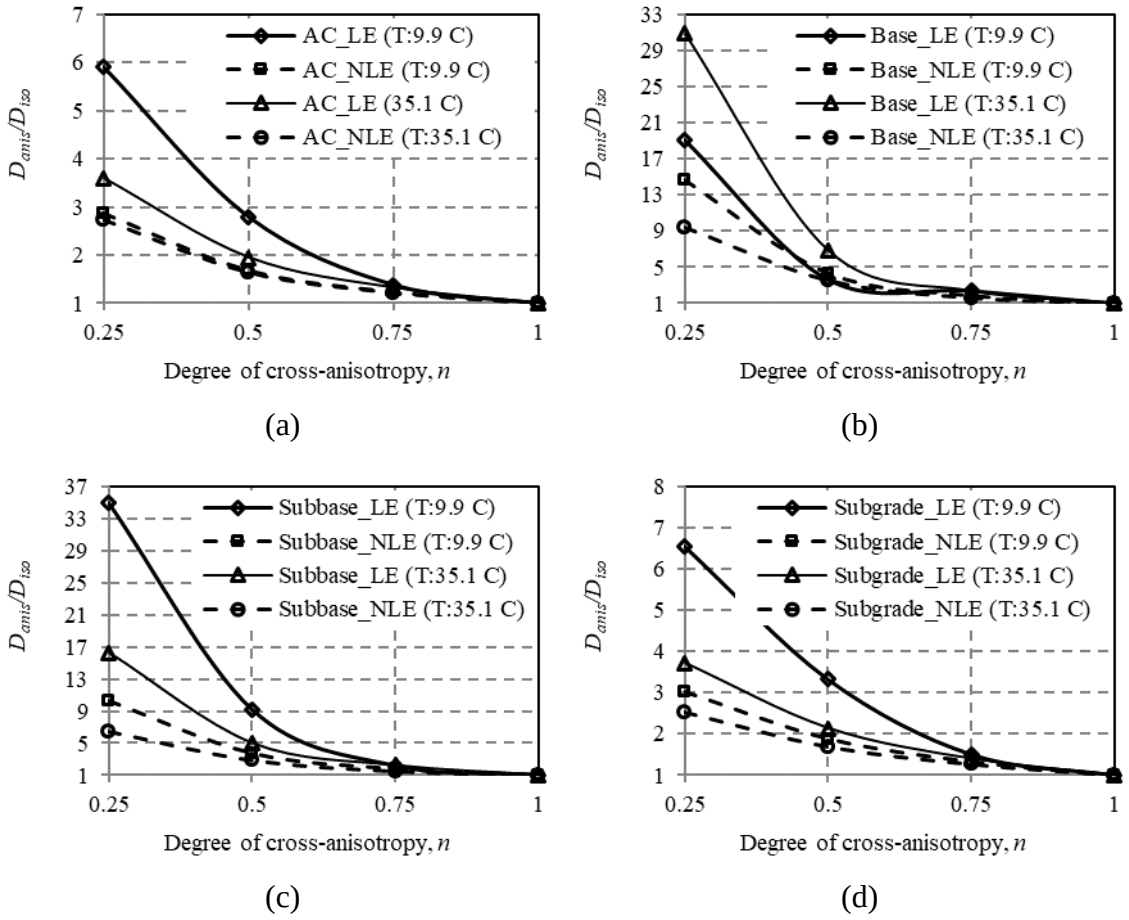

Note: LE – Linear Elastic and NLE – Non-Linear Elastic

Figure 47: Damage in: (a) AC, (b) Base, (c) Subbase, and (d) Subgrade

In summary, vertical strains in base and subbase layers based on nonlinear elasticity are greater than those based on linear elasticity. Finally, the damage based on cross-anisotropic and isotropic strain, per load repetition is high whenever the unbound layers are considered linear elastic

Effect of Loading Duration

In this step, the earlier sequence of FEM simulations at varying AC cross-anisotropy are performed by varying loading duration. Goal is to quantify the effect of loading duration on pavement stress-strain and thereby, performance. The details are discussed below:

Tensile Strain in the AC Layer — Figure 48 shows that the variation of the tensile strain with AC cross-anisotropy at different loading durations, i.e., resulted from different vehicle speed. The tensile strain decreases with increase in *n*-value of the AC as before. It is also observed that strain due to loading duration of 30 ms is slightly greater than due to 22.5 ms. This is due to the reduced relaxation modulus of the AC during the loading duration of 30 ms. The peaks of tire pressure are attained at 11.25 and 15 ms at loading durations of 22.5 and 30 ms respectively. At these specific time steps, the relaxation moduli are 2448 and 2301 ksi respectively. Therefore,

strain is smaller at of loading duration of 2448 ksi and vice versa. The different the two relaxation moduli is very small which leads to a very small difference in tensile strain.

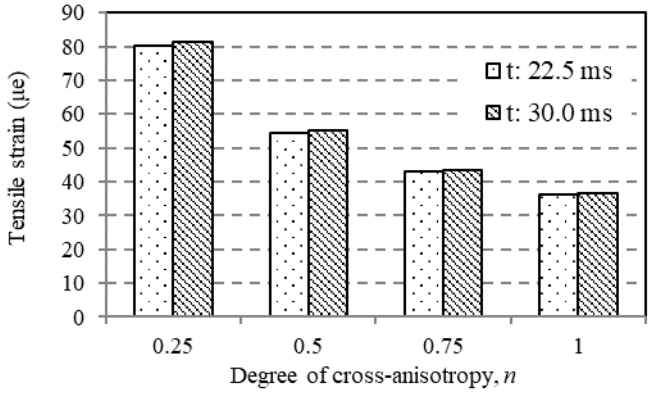

Figure 48: Tensile strain in AC layer at varying loading duration

The tensile strain ratios are calculated considering different loading durations along transverse directions since the strain along this direction is typically greater than that along longitudinal direction. The strain ratios are plotted in Figure 49(a). Strain ratios based on both loading durations decrease with *n*-value. In addition, both these trends are the same. Figure 49(b) shows the variation of the resulting damage ratio. The damage ratio also follows the similar trend of the strain ratio where it decreases with increase in *n*-values. These ratios are not affected by the variation in loading durations.

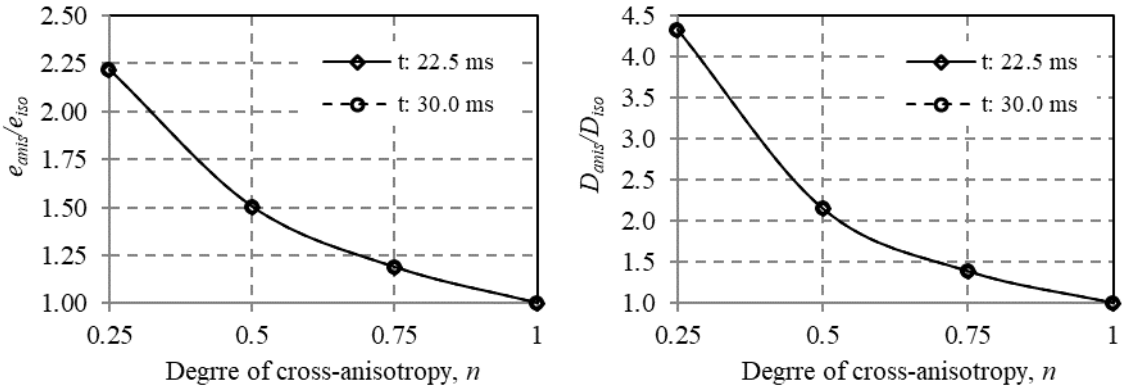

(a) Tensile strain ratio (b) Damage

Figure 49: Tensile strain ratio and damage at varying loading duration

Vertical Strains in the Pavement Layers — Figure 50(a) through (d) show the variation of vertical strains in pavement layers at varying *n*-values at the earlier mentioned loading durations. Difference in the vertical strains in the AC layer at two loading durations is very small since the difference between the relaxation moduli is also very small. However, in case of base and subbase, difference in vertical strain is high. The maximum difference is about 25 microstrain and it decreases with increase in *n*-value. This difference is resulted due to variation of vertical stresses in base and subbase, For instance, vertical stresses at mid-depth of base and subbase, i.e., 17.3 and 8.6 psi respectively, at loading duration of 30 ms which greater than those, i.e., 12.4 and

6.4 psi respectively, at loading duration of 22.5 ms. Later, the greater magnitude of stresses will lead to greater strains. In case of subgrade, vertical strain is still high due to loading duration of 30 ms. However, the difference is small which is due to very small difference in vertical stresses in this layer.

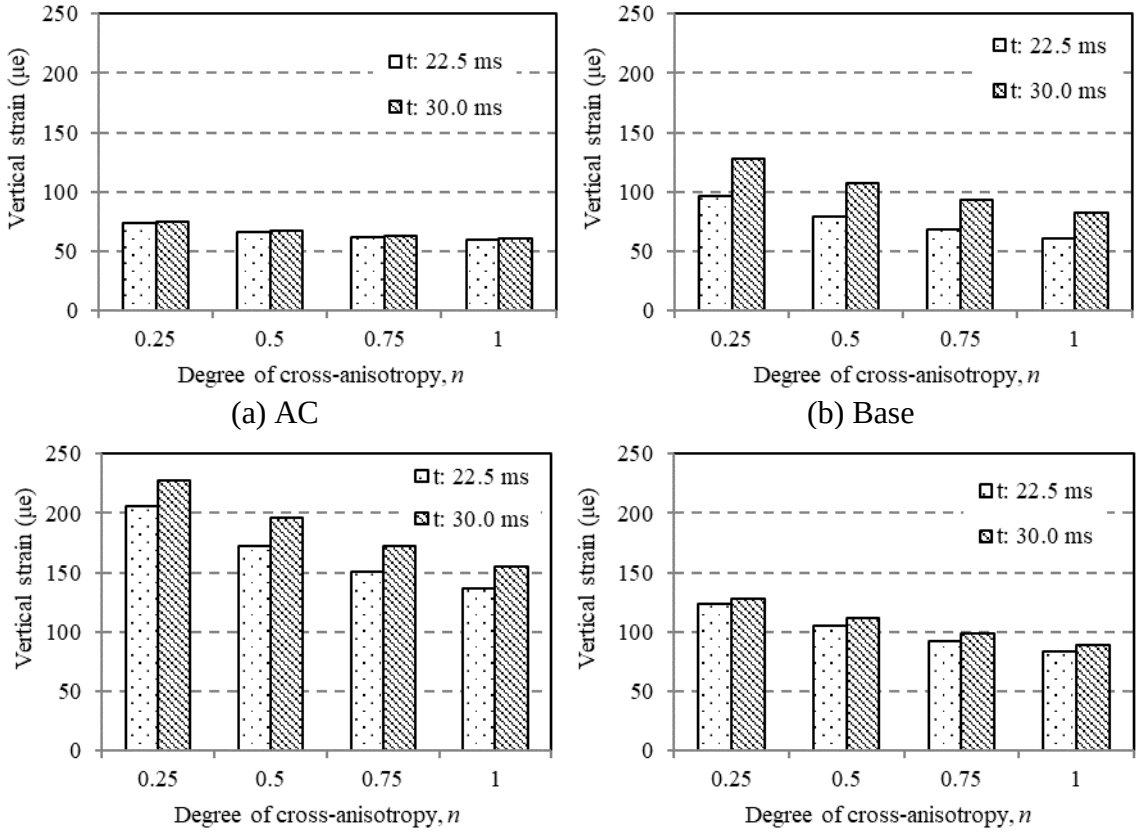

Figure 50: Vertical strain in pavement layers at varying loading duration

Figure 51(a) shows the variation of vertical strain ratios in pavement layers incorporating two different loading durations. The strain ratios decrease with increase in *n*-values as expected. In case of base and subbase, the ratio for shorter loading duration (22.5 ms) is greater than that for longer duration (30.0 ms). Strain ratios in the AC layer are not affected by the loading durations. The resulting damage is plotted against the cross-anisotropic variation in Figure 51(b). The damage ratios in the unbound layers are mainly affected by the variation in loading durations.

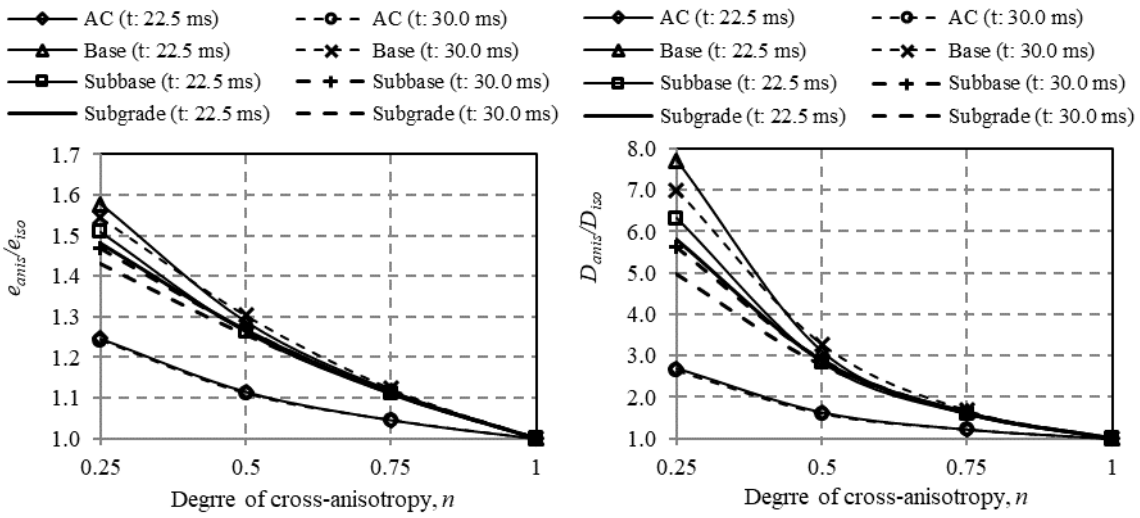

(a) Vertical strain ratio (b) Damage

Figure 51: Vertical strain ratio and damage at varying loading duration

In summary, vertical strains in the AC are barely affected by the variation in loading duration whereas these strains in unbound layers are affected by these durations. The damage ratio also follows the similar trend at the varying loading durations.

CONCLUSIONS

Goal of this study is to investigate the effect of AC cross-anisotropy on pavement responses and performances. The following conclusions are made based on the study outcomes:

- Degree of cross-anisotropy is quantified through the measurement of dynamic modulus along both horizontal and vertical directions at varying temperature and frequency. Finally, an AC material model is developed that integrates cross-anisotropy, viscoelasticity, and depth-temperature variation.
- Tensile strain at the bottom of AC layer and resulting fatigue damage is highly sensitive to AC cross-anisotropy. To be specific, tensile strain and damage is high whenever AC is cross-anisotropic instead of isotropic.
- Pavement temperature, unbound layer cross-anisotropy, and nonlinearity enhances the effect of AC cross-anisotropy on tensile strain and fatigue damage in AC layer.
- Vertical compressive strains in pavement layers are also sensitive to AC cross-anisotropy. Specially, vertical strains in unbound layers are very high in presence of AC cross-anisotropy. It leads to high increase in damage due to permanent deformation.
- Vertical strains in unbound layers and resulting damage due to permanent deformation is high in presence of high pavement temperature and base layer cross-anisotropy.
- Tensile strain and vertical strain AC layer are barely affected due to variation in loading duration. Therefore, loading duration has no influence on damage due to fatigue and permanent deformation in this layer.
- Vertical strains in unbound layers are affected by variation in loading duration. Strain is high whenever loading duration is high or in other words, slow moving vehicle is responsible for high vertical strain in unbound layers. Consequently, damage due to permanent deformation increases as loading duration increases.

RECOMMENDATIONS

Further researches on the following areas are strongly recommended to implement the concept of AC cross-anisotropy in pavement design:

- Development of calibration factors to convert pavement responses due to AC isotropy to those due to cross-anisotropy. In addition, development of charts/plots for pavement design incorporating AC cross-anisotropy.
- Advanced mechanistic modeling to investigate crack generation in AC layer and performance deformation in pavement layers under repeated traffic loading.

ACKNOWLEDGEMENT

The authors would like to acknowledge the Safety and Operations of Large-Area Rural/Urban Intermodal Systems (SOLARIS) for funding this research. Special thanks go to New Mexico Department of Transportation (NMDOT) engineers and personnel for their assistance in arranging field test. Acknowledgement is extended to the members of the Field Exploration Team, NMDOT to conduct the FWD test on the instrumented pavement section and field coring.

REFERENCES

1. Lo, S-C. R., and Lee, I. K. (1990) Response of Granular Soil along Constant Stress Increment Ratio Path. Journal of Geotechnical Engineering, ASCE. Vol. 116, No. 3, pp. 355-376.
2. Tutumluer, E. and Seyhan, U. (1999) Laboratory Determination of Anisotropic Aggregate Resilient Moduli Using an Innovative Testing Device. Transportation Research Record: Journal of Transportation Research Board, No. 1687, pp. 13-21.
3. Masad, E., Tashman, L., Somedavan, N., and Little, D. (2002) Micromechanics-Based Analysis of Stiffness Anisotropy in Asphalt Mixtures. Journal of Materials in Civil Eng., ASCE, Vol. 14, No. 5, pp. 374-383.
4. Wang, L., Hoyos, L., R., Wang, J., Voyiadjis, G., and Abadie, C. (2005) Anisotropic Properties of Asphalt Concrete: Characterization and Implications for Pavement Design and Analysis. Journal of Materials in Civil Engineering, ASCE, Vol. 17, No. 5, pp. 535–543.
5. Motola, Y., and Uzan, J. (2007) Anisotropy of Field-Compacted Asphalt Concrete Material. Journal of Testing and Evaluation, ASTM.
6. Tarefder, R. A., and Islam, M. R. (2015) Study and Evaluation of Material Response in Hot Mix Asphalt based on Field Instrumentation. Report No. NM11MSC-03, New Mexico Department of Transportation, NM, USA.
7. Abu-Farsakh, M. Y., Nazzal, M. D., and Mohammad, L. N. (2007) 2D Finite Element Analysis to Evaluate the Performance of Geogrid Base Reinforcement in Weak Flexible Pavement Structure. Intl. J. of Pavements, Vol. 6, No. 1, pp. 146-157.
8. Al-Qadi, I. L., Wang, H., and Tutumluer, E. (2010) Dynamic Analysis of Thin Asphalt Pavements Utilizing Cross-Anisotropic Stress-Dependent Properties for Granular Layer. Transportation Research Record: Journal of the Transportation Research Board, No. 10-1553, pp. 1-17.
9. Duncan, J. M., Monismith, C. L., and Wilson, E. L. (1968) Finite Element Analyses of Pavements. Highway Research Record: Journal of Highway Research Board, No. 228, pp. 18-23.
10. Petyt, M. (1990) Introduction to Finite Element Vibration Analysis. 1st Edition, Cambridge University Press, Cambridge, UK.
11. Lysmer, J., and Kuhlemeyer, R. L. (1969) Finite Element Model for Infinite Media. Journal of Engineering Mechanics, ASCE, 95(EM4), pp. 859-877.
12. Novak, M., Aboul-Ella, F., and Nogami, T. (1978) Dynamic Soil Reactions for Plane Strain Case. Journal of Engineering Mechanics Division, ASCE, Vol. 104, No. 4, pp. 953-959.
13. Gazetas, G. (1991) Formulas and Charts for Impedances of Surface and Embedded Foundations. Journal of Geotechnical Engineering, ASCE, Vol. 117, No. 9, pp. 1363-1381.
14. Shahin, M. Y., Kirchner, K., Blackmon, E. W., and Tomita, H. (1986) Effect of Layer Slippage on Performance of Asphalt-Concrete Pavements. Transportation Research Record: Journal of Transportation Research Board, No. 1095, pp. 79-85.

15. Mehta, Y. (2007) Evaluation of Interlayer Bonding in HMA Pavements. Report No: WHRP 07-07, Wisonsin Department of Transportation, WI, USA.

16. Molinari, A., Cheriguene, R., and Miguelez, H. (2012) Contact Variables and Thermal Effects at the Tool-Chip Interface in Orthogonal Cutting. International Journal of Solids and Structures, Elsevier, Vol. 49, No. 26, pp. 3774-3796.

17. Romanoschi, S. A., and Metcalf, J. B. (2001) Characterization of Asphalt Concrete Layer Interfaces. Transportation Research Record: Journal of Transportation Research Board, No. 1778, pp. 132-139.

18. Ahmed, M. U., Tarefder, R. A., and Islam, M. R. (2013) Effect of Cross-Anisotropy of Hot-Mix Asphalt Modulus on Falling Weight Deflections and Embedded Sensor Stress-Strain. Transportation Research Record: Journal of Transportation Research Board, No. 2369, pp. 20-29.

19. Siddharthan, R.V., Krishnamenon, N., El-Mously, M., and Seabaaly, P. E. (2002) Investigation of Tire Contact Stress Distribution on Pavement Response. Journal of Transportation Engineering, ASCE, Vol. 128, No. 2, pp. 136-144.

20. Al-Qadi, I. L., and Wang, H. (2009) Pavement Damage due to Different Tire and Loading Configurations on Secondary Roads. Final Report: 0081Y01, NEXTRANS Center, Indiana, USA.

21. Roque, R., Myers, L. A., and Birgisson, B. (2000) Evaluating Measured Tire Contact Stresses to Predict Pavement Response and Performance. Transportation Research Record: Journal of Transportation Research Board, No. 1716, pp. 73-81.

22. Sadd, M. H. (2009) Elasticity: Theory, Applications, and Numerics. Elsevier Inc., Burlington, MA, USA.

23. Huang, Y. H. (2004) Pavement Analysis and Design. 2nd Edition, Pearson Education Inc., New Jersey, USA.

24. Mase, G. T., and Mase, G. E. (1999) Continuum Mechanics for Engineers. 2nd Edition, CRC Press, USA.

25. Buechlar, M. A. (2012) Viscoelastic-Viscoplastic Combined Hardening Constitutive Model based on the Drucker-Prager Yield and Flow Potentials. Technical Report: LA-UR-12-24895, Los Alamos National Laboratory, NM, USA.

26. Appea, A. K. (2003) Validation of FWD Testing Results at the Virginia Smart Road: Theoretically and by Instrument Response. Ph.D. Dissertation, Virginia Polytechnic Institute and State University, Virginia, USA.

27. AASHTO (American Association of State Highway and Transportation Officials). (2015) Standard Method of Test for Determining Dynamic Modulus of Hot-Mix Asphalt Concrete Mixtures. AASHTO T 342-11, Washington, D.C.

28. Hicks, R. G., and Monismith, C. L. (1971) Factors Influencing the Resilient Properties of Granular Materials. Transportation Research Record: Journal of Transportation Research Board, No. 345, pp. 15–31.

29. Uzan, J. (1985) Characterization of Granular Materials. Transportation Research Record: Journal of Transportation Research Board, No. 1022, pp. 52–59.

30. Witczak, M. W., and J. Uzan. (1988) The Universal Airport Pavement Design System, Report I of V: Granular Material Characterization. Department of Civil Engineering, University of Maryland, College Park, MD.

31. Witczack, M. W., and El-Basyouny, M. M. (2004) Guide for mechanistic-empirical design of new and rehabilitated pavement structures. Final Report, NCHRP 1-37A, Transportation Research Board, Washington, D.C.

32. AASHTO (American Association of State Highway and Transportation Officials). (2003) Standard Method of Test for Determining the Resilient Modulus of Soils and Aggregate Materials. AASHTO T307-99, Washington, D.C.

33. Rajbongshi, P. (1997) A Critical Discussion on Mechanistic-Empirical Fatigue Evaluation of Asphalt Pavements. International Journal of Pavement Research Technology, Vol. 2, No. 5, pp. 223-226.

34. Asphalt Institute. (1982) Research and Development of the Asphalt Institute's Thickness Design Manual (MS-1). 9th Edition, Report: 82-2, Lexington, KY, USA.